Precision Engineering 43 (2016) 241–256

Contents lists available at ScienceDirect

Precision Engineering

journal homepage: www.elsevier.com/locate/precision

A high-resolution and large force-range load cell by means of nonlinear cantilever beams

Jocelyn M. Kluger, Themistoklis P. Sapsis*, Alexander H. Slocum

Department of Mechanical Engineering, Massachusetts Institute of Technology, 77 Massachusetts Avenue, Cambridge, MA 02139, United States

ARTICLE INFO

Article history:
Received 3 February 2015
Received in revised form 10 July 2015
Accepted 3 August 2015
Available online 13 August 2015

Keywords:
Nonlinear load cell
High resolution
Cantilever

ABSTRACT

In the present work, we describe a nonlinear stiffening load cell with high resolution (the ability to detect 1% changes in the force) that can function over a large force range (5 orders of magnitude), and exhibit minimal hysteresis and intrinsic geometric protection from force overload. The stiffening nature of the load cell causes its deflection and strain to be very sensitive to small forces and less sensitive to large forces. High stiffness at high forces prevents the load cell from over-straining. We physically implement the nonlinear springs with cantilever beams that increasingly contact rigid surfaces with carefully chosen curvatures as more force is applied. We analytically describe the performance of the load cell as a function of its geometric and material parameters. We also describe a method for manufacturing the mechanical component of the load cell out of one monolithic part, which decreases hysteresis and assembly costs. We experimentally verify the theory for two load cells with two different sets of parameters.

1. Introduction

Load cells are useful for applications ranging from material strength testing to prosthetic limb sensing [1], monitoring infusion pumps delivering drugs [2], agricultural product sorting [3], suction cup strength measuring [4], and human–robot collision force sensing [5].

Load cells can measure forces via several different methods, including hydraulic or pneumatic pistons and deforming materials. For hydraulic or pneumatic load cells, the force is applied to a piston that covers an elastic diaphragm filled with oil or air respectively, and a sensor converts a pressure measurement to a force measurement. Use of hydraulic load cells is limited by high cost and complexity. Pneumatic load cells are limited by slow response times and a requirement for clean, dry air [6]. The most common load cells are solid materials that deform when subject to an applied force.

Deforming load cells come in many different shapes, such as bending beams (a cantilever), S-beams (an "S"-shaped configuration of beams), single point load cells (a double-clamped beam, for which the force measurement is insensitive to the position of the load along the beam), shear beam load cells (an I-beam produces a uniform shear across its cross-section that can be measured by strain gauges), and "pancake" load cells (bending disks) [6]. All of these load cells deflect linearly.

Traditional linear load cells can be designed for almost any force capacity. Bending beam load cells are typically used for force ranges of 5.0×10^1–2.5×10^4 N and pancake load cells can be used for force ranges up to 2.5×10^6 N [6]. Many linear load cells are designed to withstand a limited amount of force overcapacity using overstops that prevent over-deflection; typically up to 50–500% load capacity before breaking [7]. Because they deform linearly, these load cells also have constant resolution (that is, the smallest force increment that they can measure) for their entire force range.

There are several challenges to designing a load cell. One wants to reduce the load cell mass and volume to minimize its effect on the test sample. Additionally, the load cell should have minimal hysteresis for accurate measurements in both up-scale and down-scale, and low side-load sensitivity (response to parasitic loads) [6]. One of the most critical design challenges is the trade-off between force sensitivity and range: It is desirable to maximize strain or deflection in the load cell in order to increase force measurement resolution because strain and deflection sensors have limited resolution; typically 14-bits between 0 and their maximum rated measurement [8–10]. Simultaneously, one wants to maximize the load cell's functional force range and protect it from breaking due to forces that exceed that range, which requires limiting its strain.

Different studies have made various modifications to the traditional linear load cell to increase its force range and sensitivity, and minimize side-load sensitivity. Chang and Lin [3] studied a "capital G-shaped" load cell with two force ranges: for small forces, a top

* Corresponding author. Tel.: +1 617 324 7508; fax: +1 617 253 8689.
E-mail address: sapsis@mit.edu (T.P. Sapsis).

http://dx.doi.org/10.1016/j.precisioneng.2015.08.003
0141-6359/

sensitive flexure deflects alone. For large forces, the sensitive flexure contacts a stiffer flexure, and the two flexures deflect together at the higher stiffness. In this way, the load cell is more sensitive to small forces and does not yield for large forces. Other devices use multiple linear load cells of increasing stiffnesses in series, as described in several U.S. patents [11,12]. The multiple load cells of a single device deflect together until overload stops prevent the weaker load cells from deflecting too far, after which the stiffer load cells continue to deflect. A microcontroller determines which load cell measurement to display. Using this approach, Storace and Sette [11] were able to measure weights over a range of 1 g to 30 kg. One way to minimize sensitivity to side-loads such as undesired moments is to use multiple load cells (i.e. 3) and take the average force measurement [11]. Challenges with these designs are that the linear load cell components have limited resolution, and using multiple load cells in one device may be bulky or expensive.

Another approach for designing a load cell with high force resolution and capacity is to use a nonlinear mechanism rather than a linear one. A nonlinear load cell may have a low stiffness at low forces (and therefore high force sensitivity) and a high stiffness at large forces (and therefore protection from yielding due to over-deflection). The design may also be volume compact and inexpensive due to requiring only one nonlinear spring and sensor per device.

A nonlinear spring may be physically realized in many different ways. The simplest form of a nonlinear spring is a cubic spring. One way to implement a cubic spring is by linear springs supporting a proof mass at various angles to its direction of travel. For example, MacFarland et al. [13] investigate a nonlinear spring realized by a thin elastic rod (piano wire) clamped at its ends without pretension that displaces transversely about its center. To leading order approximation, the stretching wire produces a cubic stiffness nonlinearity. Similarly, Hajati et al. [14] describe a spring made out of a doubly-clamped piezoelectric beam. The double-clamps cause the beam to axially stretch as it bends, resulting in a nonlinear stiffness. Mann and Sims [15] describe a spring that is implemented by a magnet sliding in a tube with two opposing magnets as the end caps. This configuration causes the stiffness to be the summation of a linear and cubic component. Kantor and Afanas'eva [16] describe the nonlinear stiffness of a clamped circular plate with variable thickness along its radius, which has a force-displacement curve similar to that of a cubic spring.

This paper describes a nonlinear stiffening load cell with high resolution (within 1% of the force value) that can function over a large range (5 orders of magnitude), with minimal hysteresis and intrinsic geometric protection from force overload. The stiffening nature of the load cell causes its deflection and strain to be very sensitive to small forces and less sensitive to large forces. When used with a constant-resolution sensor, this causes the load cell as a whole to have higher resolution for smaller forces. High stiffness at high forces prevents the load cell from over-straining. In Section 2, we develop the theory for this load cell, which uses cantilever beams that increasingly contact surfaces with carefully chosen curvatures as more force is applied. In Section 3, we describe a method for manufacturing the mechanical component of the load cell out of one monolithic part, which decreases hysteresis and assembly costs. In Section 4, we experimentally verify the theory for two load cells fabricated using the described method. Our findings are summarized in Section 5.

2. Theoretical modeling

We design the load cell as a 2×2 symmetric grid of nonlinear spring elements, as shown in Fig. 1. Load cell deflection occurs between the top and bottom rigid blocks. The nonlinear springs are physically realized by cantilevers that make contact with rigid surfaces as they deflect (splitting each cantilever length into a "segment in contact with the surface" and a "free segment"). As the contact length increases, the shortening length of the free cantilever segment causes the stiffening spring behavior. The single cantilever-contact surface nonlinear spring mechanism was first described by Timoshenko [17]. We analyze a similar nonlinear spring in Kluger et al. [18] and Kluger [19] in the context of energy harvesting from ambient vibrations. The tips of the bottom cantilevers connect to the tips of the top cantilevers by vertical rigid bars, which cannot rotate due to symmetry. To further ensure symmetry, we design the device with a rigid horizontal crossbar connecting the vertical rigid bars, as shown in Fig. 1(b), which strengthens the load cell's resistance to parasitic moments and horizontal loads. In this paper, we study load cells where the cantilever tips are either rigidly connected to these vertical bars (Fig. 1(a)) or connected to the vertical bars via moment-compliant flexures that are physically realized by three-quarters of a circular ring (Fig. 1(b)). As we show in Section 2.5, adding the 3/4-rings reduces the maximum stress in the load cell at a given applied force.

Table 1
Nomenclature for load cell components.

1/4 load cell	One of the four symmetrical spring elements, as shown in Fig. 1.
Rigid block	One of two symmetrical rigid blocks, each with four surfaces with a carefully chosen curvature.
Cantilever	One of four cantilevers with length L_{Cant}, width b, and thickness t.
Contact point, x_c	Point that separates the cantilever segment in contact with the surface and free cantilever segment and is a function of the applied force.
Cantilever segment in contact with the surface	Segment of the cantilever that is tangent to the surface, with a length from $x = 0$ to $x = x_c$.
Free cantilever segment	Segment of the cantilever that is not tangent to the surface, with a length from $x = x_c$ to $x = L$, as shown in Fig. 1.
Moment compliance ring, or 3/4-ring	270° circular arc used as a rotational spring to connect the cantilever tips to the rigid vertical bars.
Rigid connection	Junction of the cantilever tip and rigid vertical bar when the load cell does not have a 3/4-ring.
Rigid vertical bar	Component connecting the top and bottom cantilevers. It cannot rotate due to symmetry when the load cell is in pure tension/compression loadings.
Rigid crossbar	Horizontal component connecting the left and right rigid vertical bars that stiffens the load cell's response to parasitic moments and horizontal forces.
Root gap	Location of removed material near the root of the surface curve that may be required by machining limitations described in Section 3.
Root insert	Rigid blocks that follow the surface curve and can be inserted into the root gaps, described in Section 3.

Throughout this paper, we will use notation for the nonlinear spring components listed in Table 1.

We set the 1/4 surface shape to follow the curve

$$S = D\left(\frac{x}{L}\right)^n, \tag{1}$$

where $L = L_{Surf} = L_{Cant}$ is the cantilever and surface length (assuming small cantilever deflections), x measures the location along the length of the beam from its root, D is the end-gap between the surface and undeflected cantilever, and n is a power greater than 2. In theory, any curve with a monotonically increasing curvature

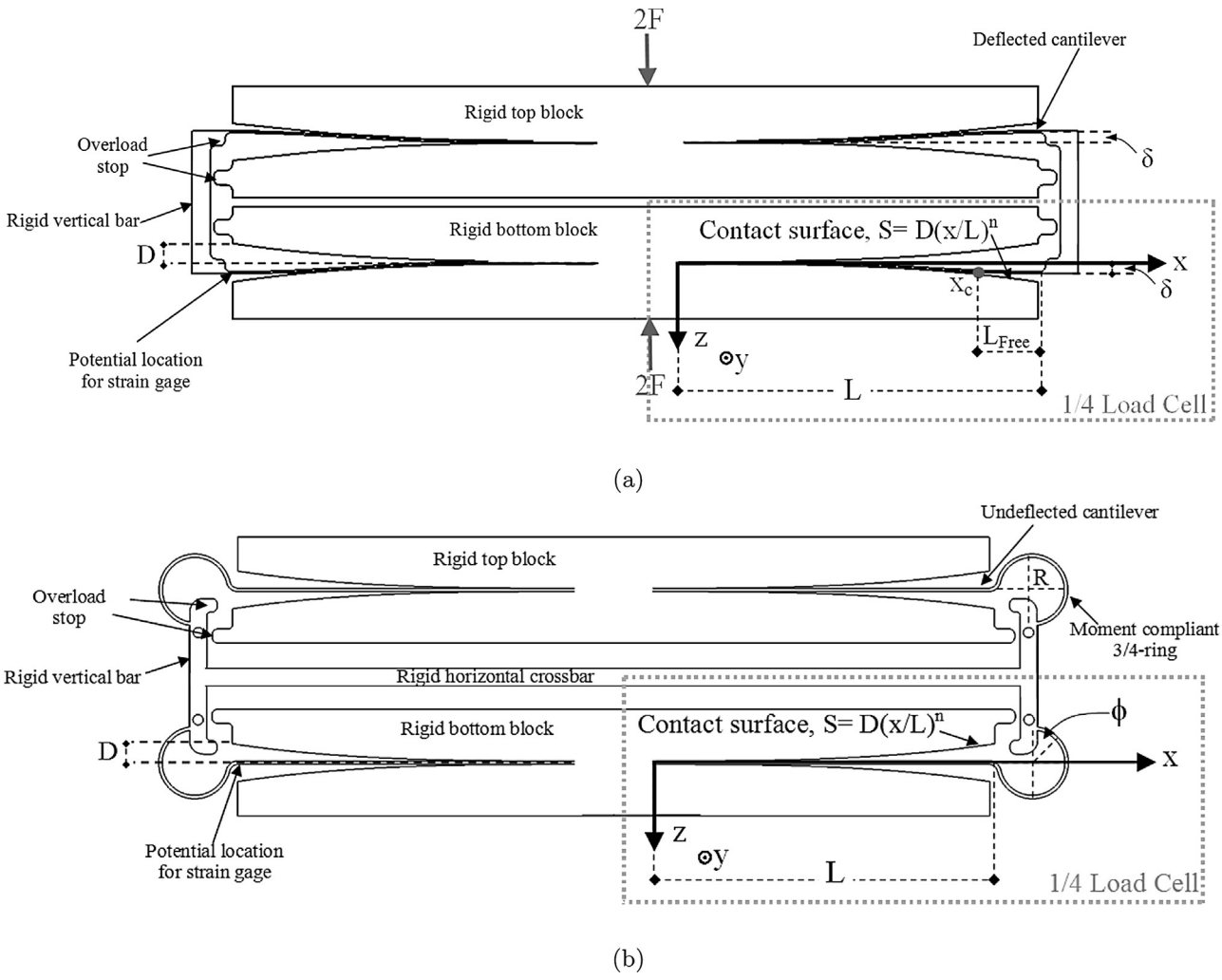

Fig. 1. (a) Load cell with rigid connections between the cantilever tip and rigid vertical bar, deflected in compression. (b) Undeflected load cell with moment compliant 3/4-rings and a rigid horizontal crossbar.

($d^2S/dx^2 > 0$) should behave similarly to the derivation described in this paper.

Below, we derive the deflection for 1/4 of the load cell with moment-complaint 3/4-rings using the Euler-Bernoulli moment-curvature relation for beams. Setting the radius of the 3/4-ring to 0 recovers the force versus deflection theory for the load cell with rigid cantilever tip connections. The full load cell's deflection is twice that of the 1/4 load cell due to the vertical stacking of the elements. The total force applied to the load cell is twice the force applied to the 1/4 load cell by the rigid side bar due to the load cell's horizontal symmetry (this can be seen by balancing the forces after making a horizontal cut through the load cell's center).

A free body diagram of the loading on the free cantilever segment is shown in Fig. 2(a). Below, we derive the load cell's force-deflection relationship when the load cell is in compression mode. The theory for tension mode is identical. Both modes cause a tensile axial force in the cantilever segment in contact with the surface due to balanced horizontal forces at the cantilever root and the contact point. As long as the surface slope is small, the horizontal force has a negligible effect on the load cell force-deflection theory.

2.1. Internal moment along the beam

We solve the boundary value problem of the internal moment in the free cantilever and 3/4-ring segments when a given force is applied downwards, as shown in Fig. 2(a), where the unknown variables are the contact point location, x_c, and value of the tip moment, M_{Tip}. The contact point, x_c, is the axial location where the cantilever stops contacting the surface and becomes a free cantilever. We assume that to the left of the contact point, the cantilever segment in contact with the surface is tangent to the surface. Therefore, for the boundary value problem, we assume that the free cantilever segment's root, x_c, is tangent to the surface (the beam and surface have equal locations and slopes). M_{x_c} is the moment and F_z is the vertical force imposed by the surface and cantilever segment in contact with the surface on the free cantilever segment at x_c that allow the load cell to be in static equilibrium. At the junction of the free cantilever segment and 3/4-ring, we require equal rotation, $\theta_{\text{Cantilever}} = \theta_{\text{Ring}}$ and moments, M_{Tip}, for continuity, as shown in Fig. 2(b) and (c). The rigid side bar applies a vertical force at the top of the 3/4-ring, point b. The rigid side bar also applies a moment, M_B, because it cannot rotate due to symmetry.

To solve this boundary value problem, we first express the internal moments in the free cantilever segment and 3/4-ring as functions of the unknown variables: the contact point x_c, and tip moment M_{Tip}, which are functions of the applied force F. Referring to Fig. 2(b), the internal moment along the free cantilever as a function of distance x from the full cantilever root is

$$M_{\text{Internal,Cant}} = -F(L - x) + M_{\text{Tip}}. \tag{2}$$

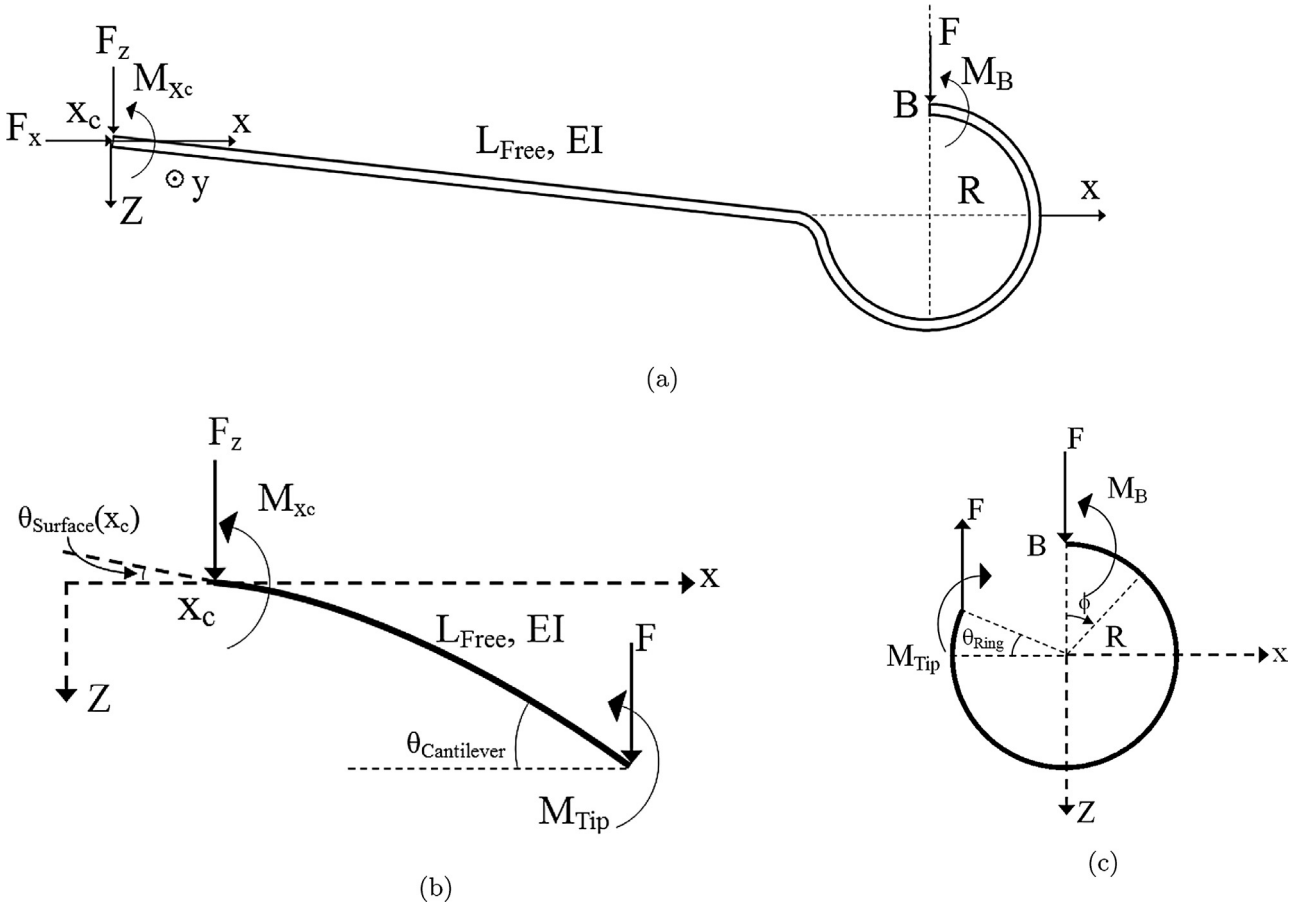

Fig. 2. (a) Free body diagram of free segment of 1/4 load cell. (b) Free cantilever segment of free body diagram. (c) 3/4-ring segment of free body diagram. The x-origin is at the full cantilever root. The free cantilever segment root is at $x = x_c$. The free cantilever segment length is $L_{\text{Free}} = L - x_c$.

Referring to Fig. 2(c), the internal moment along the 3/4-ring is

$$M_{\text{Internal,Ring}} = FR(1 + \sin\phi) + M_{\text{Tip}}. \tag{3}$$

Next, we equate the rotation at the junction of the cantilever and 3/4-ring. Since the root of the free cantilever (the contact point, x_c) is tangent to surface, it has the same angle with respect to the horizontal as the surface at that location. That is, the entire free segment of the cantilever is rotated clockwise by

$$\theta_{x_c} = \tan^{-1}\left(\frac{\mathrm{d}S}{\mathrm{d}x}|_{x_c}\right) \approx \frac{\mathrm{d}S}{\mathrm{d}x}|_{x_c}, \tag{4}$$

where we use the small angle approximation.

To find the rotation of the free cantilever segment due to bending, we use the Euler-Bernoulli beam moment-curvature relation,

$$\frac{\mathrm{d}^2 w}{\mathrm{d}x^2} = -\frac{M_{\text{Internal,Cant}}}{EI} \longrightarrow \theta_{\text{Cantilever,Bending}} \approx \frac{\mathrm{d}w}{\mathrm{d}x}|_L$$
$$= -\int_{x_c}^{L} \frac{M_{\text{Internal,Cant}}}{EI}\,\mathrm{d}x, \tag{5}$$

where we integrate the beam curvature to find the tip angle and again use the small angle approximation. $M_{\text{Internal,Cant}}$ is defined in Eq. (2).

Integrating Eq. (5), the internal moment in the free cantilever segment causes the free cantilever tip to rotate clockwise relative to its root x_c, by

$$\theta_{\text{Cantilever,Bending}} = \frac{FL_{\text{Free}}^2}{2EI} - \frac{M_{\text{Tip}}L_{\text{Free}}}{EI}, \tag{6}$$

where $L_{\text{Free}} = L - x_c$ is the free cantilever length.

To find the rotation of the 3/4-ring tip, θ_{Ring}, relative to its top (point B in Fig. 2(c)), we note the moment-curvature relation for a curved beam,

$$\frac{M_{\text{Internal,Ring}}}{EI} = \frac{1}{R_{\text{deformed}}} - \frac{1}{R_{\text{original}}} = \Delta\kappa, \tag{7}$$

where $\Delta\kappa$ is the change in beam curvature. Each infinitesimal arclength increment along the 3/4-ring rotates an infinitesimal angle, $\delta\theta \approx \Delta\kappa\ \mathrm{d}l$. Using Eq. (7), the total rotation of the 3/4-ring tip relative to point B is

$$\theta_{\text{Ring}} = \int_0^{L_{\text{Ring}}} \Delta\kappa\ \ \mathrm{d}l = \int_0^{3\pi/2} \frac{M_{\text{Internal,Ring}}}{EI} R\mathrm{d}\phi, \tag{8}$$

where the arclength $\mathrm{d}l = R\mathrm{d}\phi$, and $M_{\text{Internal,Ring}}$ is defined in Eq. (3).

Integrating Eq. (8), the internal moment in the 3/4-ring causes its tip to rotate clockwise relative to its top (point B) by

$$\theta_{\text{Ring}} = \frac{(3\pi + 2)R^2F + 3\pi RM_{\text{Tip}}}{2EI}. \tag{9}$$

Next, we equate the rotation angle at the cantilever tip (due to the surface angle at the contact point and the free length bending) to the rotation of the 3/4-ring tip (due to bending), which must be equal due to continuity,

$$\theta_{x_c} + \theta_{\text{Cantilever,Bending}} = \theta_{\text{Ring}}. \tag{10}$$

We substitute Eqs. (4), (6), and (9) into Eq. (10) and solve for M_{Tip},

$$M_{\text{Tip}} = \frac{(-3\pi R^2 - 2R^2 + L_{\text{Free}}^2)F + 2\frac{\mathrm{d}S(x_c)}{\mathrm{d}x}EI}{3\pi R + 2L_{\text{Free}}}. \tag{11}$$

Eq. (11) expresses M_{Tip} as a function of the applied force, F, and contact point, x_c (because $L_{Free} = L - x_c$ and $\frac{dS(x_c)}{dx}$ are both functions of x_c). In Section 2.2, we determine x_c as a function of F and M_{Tip}.

Eq. (11) also shows that for a load cell in compression, when $L > \sqrt{3\pi + 2}\ R$, M_{Tip} is positive for small forces but becomes negative for large forces (as L_{Free} decreases). If $L < \sqrt{3\pi + 2}\ R$, then M_{Tip} is negative for any applied force. Physically, a positive M_{Tip} represents how for small forces, the 3/4-ring applies a moment to the cantilever tip that counteracts the cantilever's bending due to the applied force. Simultaneously, the cantilever tip applies a moment to the 3/4-ring at $\phi = 3\pi/2$ in the direction that causes its radius to decrease (overall, the 3/4-ring deflects downwards because of the directly applied force). For large forces (when the free cantilever has stiffened due to a shorter length) or for load cells with sufficiently small L:R ratios, the cantilever applies a moment to the 3/4-ring at $\phi = 3\pi/2$ in the direction that increases its radius, and the 3/4-ring applies a moment to the cantilever that pushes the cantilever tip in the same direction as F. This is caused by the 3/4-ring deflecting downwards with respect to $\phi = 3\pi/2$ and the free cantilever becoming stiffer. When the load cell is in tension, the notation has negated signs and the components move in opposite directions, but the theoretical relationships remain identical.

2.2. Cantilever contact point with surface

We determine the value of the contact point x_c, for a given force by setting the surface curvature equal to the beam curvature at the contact point. This is the contact condition because we assume that the beam segment in contact with the surface is tangent to the surface (matching curvature). At the contact point, the cantilever curvature must be continuous because there is not an applied external moment at the contact point. Using the expression for the internal moment given by Eq. (2), the contact condition becomes:

$$\frac{d^2S}{dx^2}|_{x_c} = \frac{M_{Internal,Cant}}{EI}|_{x_c} \longrightarrow \frac{d^2S}{dx^2}|_{x_c} = \frac{F(L - x_c) - M_{Tip}}{EI}, \tag{12}$$

where M_{Tip} is the function of F and x_c given by Eq. (11). The contact point for a given force can be determined by substituting Eqs. (1) and (11) into Eq. (12) and solving for x_c.

For general surfaces, Eqs. (11) and (12) can be simultaneously numerically solved for a given force. When the surface has a constant radius of curvature ($n = 2$ in Eq. (1)), the left hand side of Eq. (12) is a constant, and the equation can be explicitly solved for the contact point and tip moment for a given force, as described in Section 2.5.1. After determining the contact point x_c, and tip moment M_{Tip}, for a given force, we can calculate the load cell deflection.

2.3. Deflection

For a given applied force, the deflection of the 1/4 load cell indicated in Fig. 1 relative to the rigid block is the summation of four components:

$$\delta = \delta_1 + \delta_2 + \delta_3 + \delta_4. \tag{13}$$

The first component is the beam deflection at the contact point, x_c. This deflection component is the vertical location of the surface curve at x_c,

$$\delta_1 = S(x_c). \tag{14}$$

The second component is the deflection of the free part of the beam due to the beam's slope at the contact point. Since the beam is tangent to the surface at the contact point, its slope equals the surface slope. The free length of the beam rotates by this slope (i.e. small angle) about the contact point, which results in the deflection,

$$\delta_2 = \frac{dS}{dx}|_{x_c} L_{Free}, \tag{15}$$

where $L_{Free} = L - x_c$ is the length of the free cantilever, assuming small deflections.

The third deflection component is due to the free cantilever bending. This can be found by integrating the moment-curvature relation, Eq. (5), twice and using boundary conditions that the deflection and slope due to bending equal zero at the free beam's root (the contact point, x_c). This deflection component is:

$$\delta_3 = \frac{FL_{Free}^3}{3EI} - \frac{M_{Tip}L_{Free}^2}{2EI}. \tag{16}$$

The fourth deflection component is due to the 3/4-ring bending. When an infinitesimal segment of the 3/4-ring, $\delta l = R\mathrm{d}\phi$, bends, it rotates the segments of the ring on either side of it by an angle $\delta\theta = \Delta\kappa\ \delta l$ with respect to each other, where $\Delta\kappa$ is the change in the curvature of the beam at the infinitesimal segment due to bending. Based on geometry and the small angle approximation, the vertical tip deflection due to this change in angle is the horizontal distance between the infinitesimal segment and the 3/4-ring tip, $X = R(1 + \sin\phi)$, multiplied by the change in angle, $\delta\theta$. Integrating this infinitesimal deflection along the 3/4-ring results in the total deflection of the 3/4-ring due to bending:

$$\delta_4 = \int_{l_{Curve}} X\ \ \delta\theta\ \ = \int_0^{\frac{3\pi}{4}} R(1 + \sin\phi)\ \ \Delta\kappa\ \ R\mathrm{d}\phi$$

$$= \int_0^{\frac{3\pi}{4}} R^2(1 + \sin\phi)\ \ \frac{M_{Internal,Ring}}{EI}\ \ \mathrm{d}\phi, \tag{17}$$

where the change in curvature of the beam, $\Delta\kappa$ is caused by the internal moment defined in Eq. (3). Substituting in Eq. (3) for $M_{Internal,Ring}$ and integrating the right hand side of Eq. (17), the deflection of the 3/4-ring top (point b) with respect to the cantilever tip is:

$$\delta_4 = \frac{(9\pi + 8)FR^3 + (6\pi + 4)M_{Tip}R^2}{4EI}. \tag{18}$$

As expressed in Eq. (13), the deflection of the 1/4 load cell is the summation of the deflection components given by Eqs. (14)–(16), and (18), where x_c and M_{Tip} for a given force, F, are found by simultaneously solving Eqs. (11) and (12). We multiply the applied force F, and deflection δ, of the 1/4 load cell by 2 to determine the applied force $2F$, and deflection 2δ, of the entire load cell.

2.4. Stress

For a load cell that will undergo repeated cycles of stress, ensuring that the maximum stress is below a certain value will prevent yield and extend the load cell's fatigue lifetime. The normal stress, σ, of a thin beam is related to its strain, ε, by $\sigma = E\varepsilon$, where E is the elastic modulus of the beam material. This stress formula is valid for curved beams with $R \gg t/8$, where t is the thickness of the beam's cross-section relative to the neutral axis [20]. For a beam in pure bending, the strain relates to the beam's change in curvature, $\Delta\kappa$ (defined in Eq. (7)), by $\epsilon = \Delta\kappa t/2$. In the free segments of the load cell, $\Delta\kappa$ relates to the internal moment by $M_{Internal} = EI\Delta\kappa$, where I is the beam's moment of inertia about its neutral axis. Combining these expressions, the normal stress in the cantilever can be expressed as $\sigma = Et\Delta\kappa/2$ or $\sigma = Mt/2I$.

The stress along the cantilever and 3/4-ring for a given applied force is defined by several equations. For the cantilever segment in

contact the surface, the cantilever curvature equals the surface curvature ($\Delta\kappa = \frac{d^2S}{dx^2}$) because the cantilever is tangent to the surface. The surface shape, $S(x)$, is given by Eq. (1). Substituting Eq. (1) into $\sigma = Et\Delta\kappa/2$, the cantilever segment in contact with the surface has stress:

$$\sigma_{\text{InContact}} = E\frac{t}{2}\frac{Dn(n-1)}{L^n}x^{n-2}, \tag{19}$$

where x is the axial distance along the cantilever from its root and the load cell parameters are labeled in Fig. 1. When the load cell is in compression, the cantilever of the South East 1/4-load cell indicated in Fig. 1 contacts the surface below it, and the top of this beam segment is in tension. When the load cell is instead in tension, this beam segment contacts the surface above it, and the top of the beam segment is in compression.

For the free cantilever segment ($x_c < x < L$), the internal moment is defined in Eq. (2). Substituting the expression for internal moment into $\sigma = Mt/2I$, the stress along the top of the beam (for the indicated 1/4 load cell in Fig. 1) is:

$$\sigma_{\text{Straight,Free}} = \frac{t}{2I}\left(F(L-x) - M_{\text{Tip}}\right) \tag{20}$$

If the surface has nonlinearity, $n = 2$, then the load cell deflects a certain distance before the cantilever contacts the surface, and the equation for stress along the beam is found by substituting $x_c = 0$ into Eq. (20), where M_{Tip} is a function of x_c.

Eq. (19) shows that when the surface has $n > 2$, the stress increases along the beam length, x, in the cantilever segment in contact with the surface because the surface curvature increases along x. When $n = 2$, the stress is constant in the cantilever segment in contact with the surface because the surface has a constant curvature. Eq. (20) shows that in the free cantilever segment, the stress decreases along the axis, x, and may become negative. The cantilever curvature must change from positive to negative to satisfy the 0-slope tip condition when $R/L = 0$. When $R/L > 0$, the moment applied by the moment compliant 3/4-ring on the cantilever tip decreases the tip curvature but does not require it to become negative.

Therefore for a given force, the maximum stress in the cantilever occurs at the contact point, as we will show in Fig. 6 in Section 2.5.2. (Here, we use the sign conventions for the top of beam in the South-East 1/4 load cell when the load cell is in compression.) The stress at the contact point is given by:

$$\sigma_{x_c} = E\frac{t}{2}\frac{Dn(n-1)}{L^n}x_c^{n-2} = \frac{t}{2I}((L-x_c)F - M_{\text{Tip}}), \tag{21}$$

where Eq. (21) is found by substituting $x = x_c$ into Eqs. (19) and (20). Since the contact point moves to the right as the applied force increases and the surface curvature increases to the right, the stress at the contact point increases as more force is applied. The minimum stress in the cantilever occurs at the cantilever tip (found by substituting $x = L$ into Eq. (20)) or at the full cantilever root. When the load cell has moment compliant 3/4-rings, sufficiently large forces cause the entire cantilever to contact the surface, and the stress at $x = L$ is defined by Eq. (21) when $x_c = L$. When the load cell has rigid connections instead of 3/4-rings, the load cell will break before the tip becomes tangent to the surface because continuity would require the tip slope to both equal 0 and be tangent to the surface.

When the load cell has moment compliance 3/4-rings, the stress along the inside radius of the 3/4-ring is

$$\sigma_{\text{Ring}} = \frac{-t}{2I}(FR(1+\sin\phi) + M_{\text{Tip}}(x_c)). \tag{22}$$

Eq. (22) shows that there are two extrema in the stress along the 3/4-ring. At $\phi = \pi/2$, the stress is

$$\sigma_{\text{Ring}}|_{\phi=\pi/2} = \frac{-t}{2I}\left(2FR + M_{\text{Tip}}(x_c)\right). \tag{23}$$

At $\phi = 3\pi/2$, the stress is

$$\sigma_{\text{Ring}}|_{\phi=3\pi/2} = \frac{-t}{2I}\left(M_{\text{Tip}}(x_c)\right). \tag{24}$$

We note that $\phi = 3\pi/2$ is the same point as $x = L$, and the equations above result in the same internal moment and stress at these two points. For small forces, the stress magnitude is larger at $\phi = \pi/2$ than at $\phi = 3\pi/2$. Equating Eqs. (23) and (24), the stress magnitude at $\phi = 3\pi/2$ exceeds the stress magnitude at $\phi = \pi/2$ when $F = -M_{\text{Tip}}/R$ (M_{Tip} becomes negative as described in the last paragraph of Section 2.1).

For the reasons described above, when designing the load cell to have a specific safety factor against yield, there are several possible locations to check for the maximum stress magnitude. These points are the cantilever root ($x = 0$; applicable only when $n = 2$ and before the cantilever has begun contacting the surface. This stress is found using Eq. (20) when $x_c = 0$), the contact point ($x = x_c$, Eq. (21)), the cantilever tip ($x = L$, Eq. (20) or $\phi = 3\pi/2$, Eq. (24)), and $\phi = \pi/2$ on the 3/4-ring (Eq. (23)). To check the stress at these points, one must know x_c and M_{Tip} as a functions of the applied force (see Eq. (11) and Section 2.2). The relative magnitudes of the stresses along the load cell flexures depends on the ratio of cantilever length to 3/4-ring radius, $L{:}R$, and the contact point value, x_c. Section 2.5 further illustrates the effect of parameters on the stress.

2.5. Effect of parameters on load cell performance

We measure a load cell's performance by its force-measurement resolution and force range. Resolution, the smallest force increment that the load cell can distinguish, is limited by the load cell stiffness (or strain gradient with respect to the applied force) and the resolution of the sensor that converts the load cell displacement (or strain) into an electrical signal.

Typical sensors can distinguish 14-bits (2^{14} increments) between 0 and full-scale deflection (or strain), after accounting for sensor noise [8–10]. If the load cell uses a single optical or eddy-current sensor and one wants the load cell to resolve the entire load cell force, $2F$, to within $100P\%$ of its current value, then there is a limit to the maximum allowable load cell stiffness at each force. We assume that the sensor is sized for maximum sensitivity in the deflection range so that its resolution is $res_{\text{Sensor}} = \frac{2\delta_{\text{Max}}}{2^{14}}$. At a given force, $2F$, the load cell stiffness is defined as $K = \frac{d(2F)}{d(2\delta)}$. For this stiffness, a small change in the applied force causes a small change in the deflection: $d(2\delta) = \frac{d(2F)}{K}$. For the desired resolution, when the change in force is $d(2F) = P \times 2F$, we require the change in deflection, $d(2\delta)$, to be larger than the smallest deflection increment that the sensor can detect: that is $res_{\text{Sensor}} \le \frac{2FP}{K}$. Rearranging this expression, for a force measurement resolution of $100P\%$ of the applied force $2F$, the maximum allowable load cell stiffness as a function of the applied force is

$$K_{\text{SingleSensor}} \le \frac{2^{14}(2F)P}{2\delta_{\text{Max}}}. \tag{25}$$

For increased resolution, one may use multiple optical or eddy-current sensors on a single load cell that are active in different deflection ranges. For example, the highest resolution for typical optical sensors is 1×10^{-7} m, when they have displacement ranges of 2.5 mm [9,10]. Two of these 2.5 mm deflection sensors could be used for a load cell with a 5 mm deflection range: the structure may be designed so that when the load cell deflects between 2.5 and 5 mm, the gap between the upper-range sensor and its target is

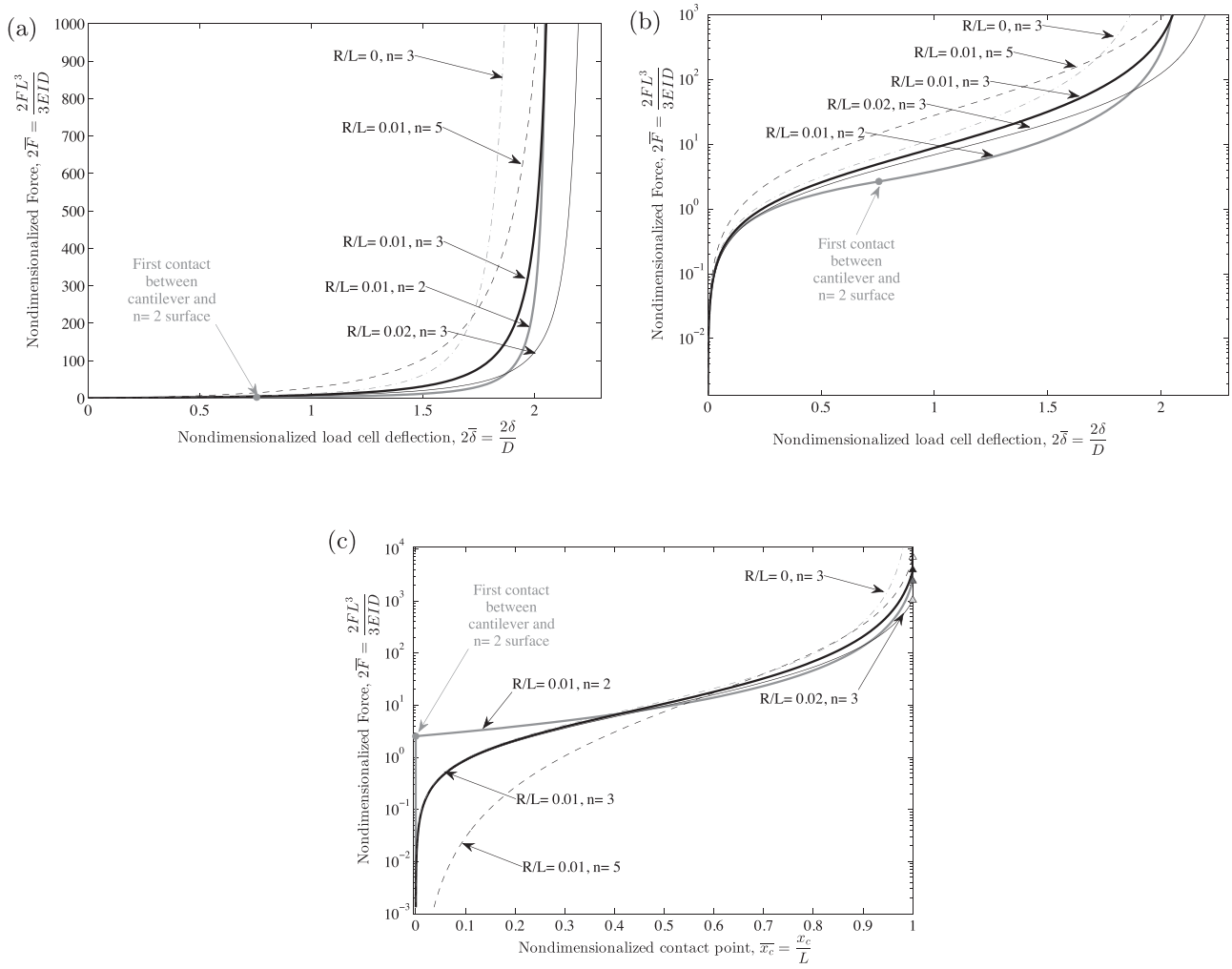

Fig. 3. (a) Nondimensionalized theoretical force versus deflection. (b) Nondimensionalized theoretical force versus deflection with a log force scale. (c) Contact point between cantilever and surface for varied parameters.

between 0 and 2.5 mm. Of course, using multiple sensors increases the device cost.

When daisy-chaining multiple high resolution sensors in this way and using sensors that can resolve 0.1 μm, then for 100*P*% force resolution, we require a change in displacement per force: $\frac{d(2\delta)}{d(2F)} \geq \frac{10^{-7}m}{P \times 2F}$, or stiffness,

$$K_{\text{MultipleSensors}} = \frac{d(2F)}{d(2\delta)} \leq \frac{2FP}{10^{-7}}. \tag{26}$$

If the applied force is $F = 0.01$ N [1 g], and one desires $100P = 1\%$ force resolution, then it is desirable to have a stiffness of $K = \frac{d(2F)}{d(2\delta)} \leq 1000$ N/m. If $F = 1,000$ N [100 kg], it is desirable to have $K \leq 1e8$ N/m.

If the load cell uses a strain gauge with 14-bit resolution instead of a displacement sensor, then the smallest strain increment that an analog-to-digital converter can distinguish is $\varepsilon_{\text{Res}} = \frac{\varepsilon_{\text{Max}}}{2^{14}}$, when the gauge and Wheatstone bridge are sized for the maximum strain and we assume the maximum strain is on the order of 1000 $\mu\varepsilon$, which is the optimal range for strain gauges and strain limit for a long fatigue life in aluminum or steel load cells [7]. Then, to detect a 100*P*% change in force, the requirement on the strain gradient with respect to the applied force is

$$\frac{d\varepsilon}{d(2F)} \geq \frac{\varepsilon_{\text{Res}}}{P \times 2F} \longrightarrow \frac{d\varepsilon}{d(2F)} \geq \frac{\varepsilon_{\text{Max}}}{2^{14}P \times 2F}. \tag{27}$$

In addition to resolution limitations, load cell force range is limited by the stress: stress at any point in the cantilever or 3/4-ring cannot exceed the material yield stress. At large forces, load cells with lower stiffnesses deform more and consequently have larger stress than stiffer load cells at the same force. On the other hand, load cells that are too stiff deflect too little for high force measurement resolution. Therefore, optimal load cell performance is a trade-off between force range (not bending too much) and force accuracy (not bending too little). To maximize both force resolution and range, it is optimal to design the load cell so that its stiffness is just below the maximum allowable value or strain just above the minimum allowable value for a desired measurement resolution.

In Section 2.5.1, we analytically derive the equations relating geometric and material parameters to the performance of a load cell with a constant-curvature surface. In Section 2.5.2, we discuss the effect of varied parameters on load cells with general surfaces. Figs. 3–8 illustrate the load cell performance for varied nondimensionalized parameter ratios.

2.5.1. Surface with a constant radius of curvature

When the surface nonlinearity is $n = 2$, the expression for the surface shape, Eq. (1) can be rewritten as

$$S = D\left(\frac{x}{L}\right)^2 = \frac{x^2}{2R_{\text{Surf}}}, \tag{28}$$

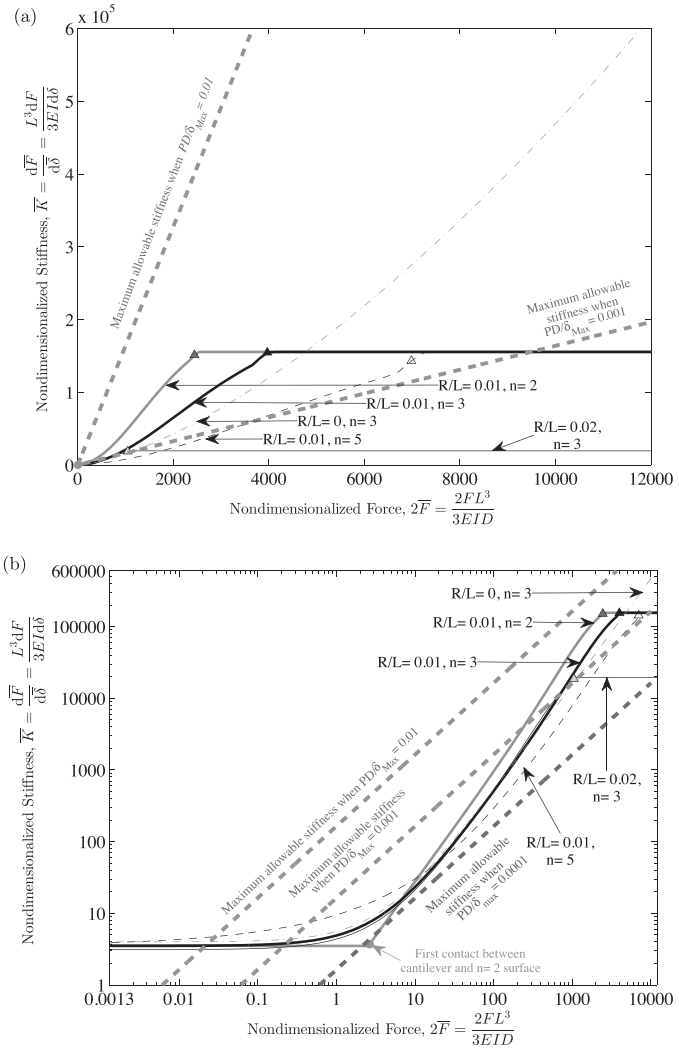

Fig. 4. Nondimensionalized theoretical load cell stiffness versus force for varied parameters. (a) Linear scaling. (b) Log scaling. The maximum allowable stiffness lines represent the stiffness limits for 100*P*% force resolution of the applied force for a displacement sensor with 14-bit effective resolution, with a displacement range of 0 m to δ_{Max}.

where $d^2S/dx^2 = 1/R_{Surf}$ is the surface's constant curvature along its axis.

This constant curvature greatly simplifies the equations for the nonlinear load cell behavior and allows for analytic expressions relating the applied force F, tip moment M_{Tip}, and contact point x_c. Simultaneously solving Eqs. (11) and (12) (using Eq. (28) for S) for the relationship of F, x_c, and M_{Tip} results in

$$F = \frac{EI\,(3\pi R + 2L)}{R_{Surf}\left((3\pi+2)R^2 + 3\pi R(L-x_c) + (L-x_c)^2\right)} \tag{29}$$

and

$$M_{Tip} = \frac{\left((-3\pi-2)R^2 + L^2 - x_c^2\right)EI}{R_{Surf}\left((3\pi+2)R^2 + 3\pi R(L-x_c) + (L-x_c)^2\right)}. \tag{30}$$

Eqs. (29) and (30) define the applied force on the 1/4 load cell and moment at the cantilever tip-3/4-ring junction (labeled in Figs. 1 and 2) as functions of the contact point between the

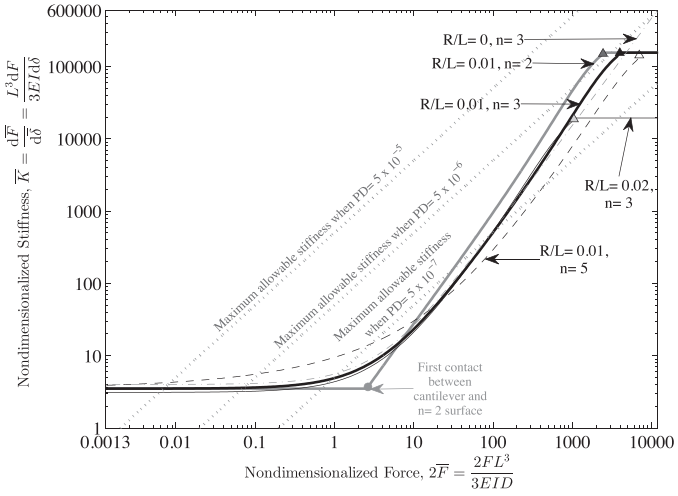

Fig. 5. Nondimensionalized theoretical load cell stiffness versus force, log scaling. The maximum allowable stiffness lines represent the stiffness limits for 100*P*% force resolution at the applied force for a displacement sensor with 0.1 μm resolution, independent of sensor range.

cantilever and surface, x_c. When the 3/4-ring radius, $R = 0$ (in addition to $n = 2$), the contact point equation, Eq. (29), simplifies to

$$x_c = L - \sqrt{\frac{2LEI}{R_{Surf}F}}. \tag{31}$$

Eq. (31) shows that as the force, F, increases, the point of contact between the cantilever and surface, x_c, approaches the cantilever length, L. When $R = 0$, the expression for M_{Tip}, Eq. (30), also simplifies to

$$M_{Tip} = \frac{L_{Free}^2 F + 2\frac{dS(x_c)}{dx}EI}{2L_{Free}}, \tag{32}$$

where $L_{Free} = L - x_c$, and x_c is the function of F defined in Eq. (31).

Then, the deflection equation, Eq. (13), simplifies to

$$\delta = \frac{FL_{Free}^3}{12EI} + \frac{S'(x_c)L_{Free}}{2} + S(x_c), \tag{33}$$

where again x_c is defined in Eq. (31).

Please note that the values of F and δ in Eqs. (31)–(33) are for the quarter-load cell. They are actually one-half the applied force and deflection of the entire load cell.

2.5.2. Discussion of effect of parameters on general surfaces

Many geometric and material parameters may be adjusted to optimize the load cell performance. These parameters include the cantilever's elastic modulus E, length L, width b, and thickness t; the 3/4-ring radius R; and the surface nonlinearity power n and end-gap D; as labeled in Fig. 1.

The 3/4-ring width and thickness may also be adjusted independently of the cantilever width and thickness. Increasing either of these dimensions increases the 3/4-ring rotational stiffness, which has a similar effect to decreasing R. For simplicity in this analysis, we assume that the 3/4-ring width and thickness remain equal the cantilever width and thickness.

It can be shown that the force, deflection, stiffness, contact point, stress, and strain nondimensionalize to

$$2\bar{F} = \frac{2FL^3}{3EID}, \tag{34}$$

$$2\bar{\delta} = \frac{2\delta}{D}, \tag{35}$$

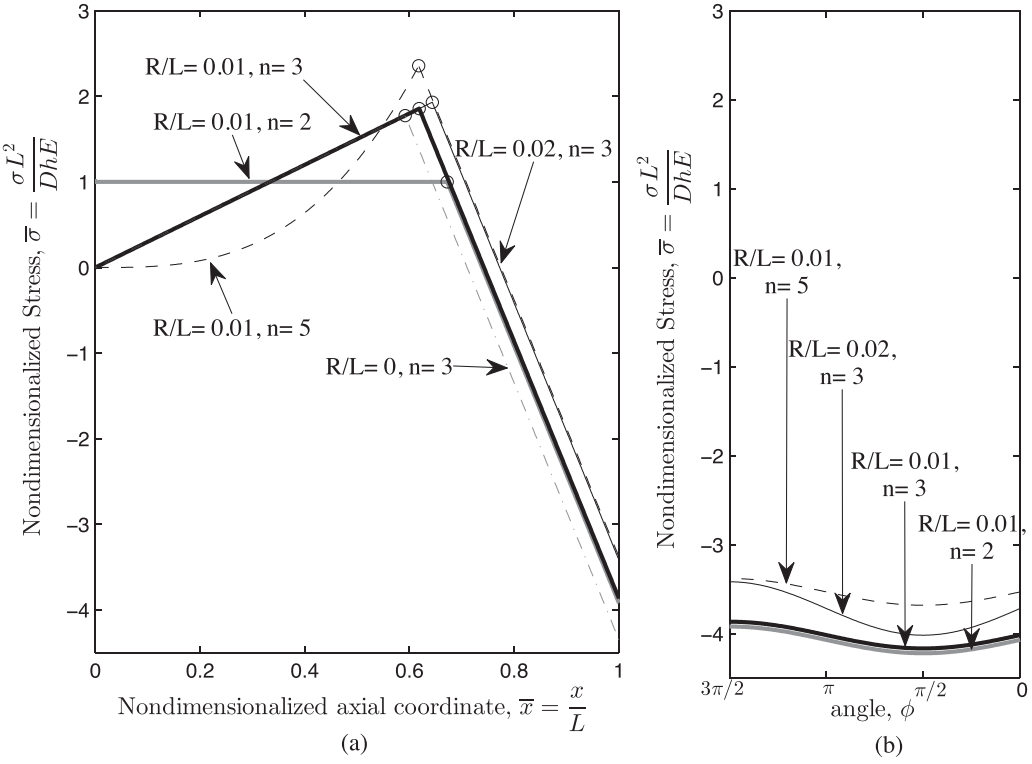

Fig. 6. Nondimensionalized theoretical normal stress along the cantilever and 3/4-ring when $2\bar{F} = 30$ is applied to the load cell for varied parameters.

$$\bar{K} = \frac{\mathrm{d}(2\bar{F})}{\mathrm{d}(2\bar{\delta})} = \frac{L^3}{3EI}\frac{\mathrm{d}F}{\mathrm{d}\delta}, \tag{36}$$

$$\bar{x} = \frac{x}{L}, \tag{37}$$

$$\bar{\sigma} = \frac{\sigma L^2}{DtE}, \tag{38}$$

$$\bar{\varepsilon} = \frac{\varepsilon}{\varepsilon_{\bar{x}_c=0.9}}, \tag{39}$$

where we use the coefficient of 2 in Eqs. (34) and (35) to represent the entire load cell deflection and applied force (whereas the previous analysis in Section 2 examined F and δ for only the 1/4 load cell indicated in Fig. 1). Eq. (34) shows that the force required for a given deflection increases proportionally with the cantilever stiffness (where a cantilever's stiffness is $3EI/L^3$. $EI = Ebt^3/12$ is the cantilever rigidity, and L is its length). Eq. (35) shows that the deflection for a given force increases proportionally with the surface end-gap, D. Eq. (38) shows that increasing the cantilever length, L, decreases the stress for a given deflection, while increasing the cantilever thickness, t, elastic modulus, E, or surface end-gap, D, increases the stress. In Eq. (39), we choose to normalize the strain by the strain at the cantilever tip when 90% the beam length is in contact with the surface. We choose to normalize the strain this way so that if the cantilever is roughly 10 cm long, then $0.1L = 1$ cm is roughly the allowable space for adhering a strain gauge to the cantilever tip. For other studies and applications, ε could be normalized by another factor.

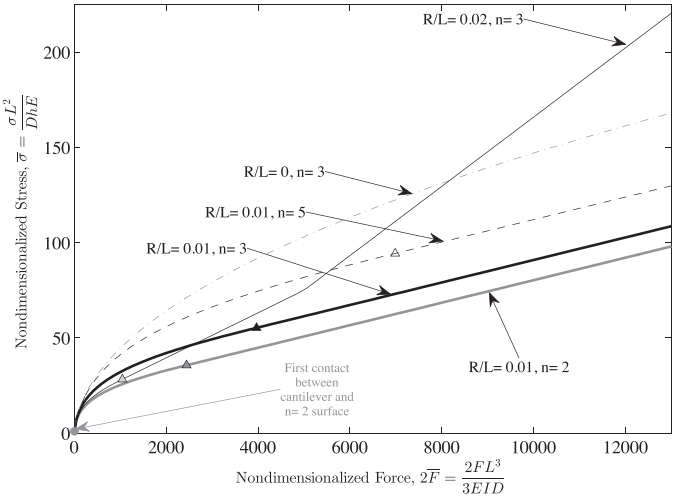

Fig. 7. Nondimensionalized theoretical maximum stress magnitude versus applied force for varied parameters.

Figs. 3–8 show the effect of the surface nonlinearity, n, and ratio of the 3/4-ring radius to straight beam length, R/L, on the nondimensionalized load cell performance.

Fig. 3(a) and (b) shows the theoretical nondimensionalized force versus deflection. For all parameter sets, the force suddenly approaches very large values as the cantilever approaches the critical deflection value, D (the load cell reaches the deflection value $2D$). The physical reason for this sudden increase is that at large enough forces, the entire cantilever length contacts the surface, and the tip cannot deflect any further. The surface nonlinearity, n, defines the smoothness of the transition to very large force values. Specifically, for small values of n, the load cell force suddenly grows very large close to the critical value of deflection, D. For larger values of n, there is a smooth transition to the large-force regime.

The ratio R/L determines the slope of the asymptotic line approached by the force versus deflection curve at large forces. For $R/L = 0$, the asymptotic line is vertical: the load cell deflection cannot exceed $2D$ because the only flexible elements of the structure, the cantilevers, each deflect to D when their entire lengths are in contact with the rigid surfaces. For larger R/L, the force versus deflection curve asymptote has a slope equal to the 3/4-ring stiffness. This is

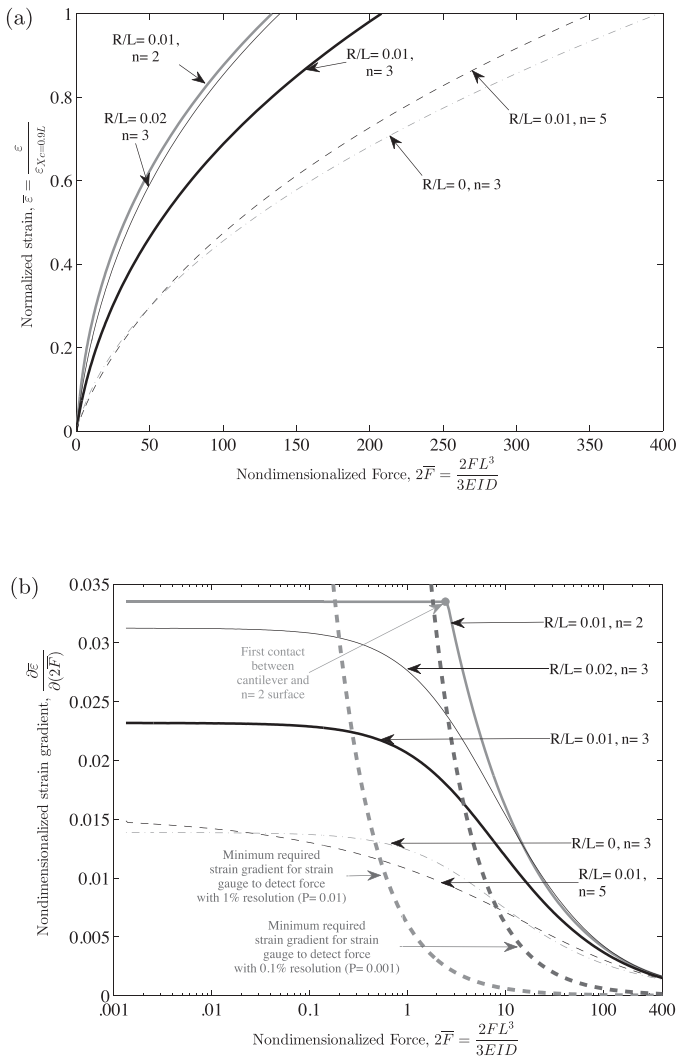

Fig. 8. (a) Theoretical strain versus force at the cantilever tip (strain gauge location 1 labeled in Fig. 1). The strain is normalized by the strain at location 1 when the 90% of the cantilever length is in contact with the surface ($x_c = 0.9L$). (b) Theoretical gradient of the strain with respect to the nondimensionalized force.

because as $\bar{x}_c \longrightarrow 1$, the load cell deflection is effectively due to the 3/4-rings deflecting alone.

Fig. 3(c) shows the theoretical nondimensionalized cantilever-surface contact point versus force. For the $n = 2$ surface, contact does not begin ($\bar{x}_c > 0$) until a critical force is reached. Before this critical force, the load cell behaves linearly. For larger n surfaces, the contact point is larger for a given small force and smaller for a given large force. This is because as n increases, the surface shape is flatter near the root and rounder near the tip. Where the surface is flatter (larger n and near the root), the contact point increases more for a given increase in the applied force. Where the surface is rounder (smaller n and near the tip), the contact point increases less for the same increase in applied force.

Increasing the R/L ratio increases the contact point for any given force (until the contact point becomes and remains $\bar{x}_c = 1$). This is because increasing R/L decreases the stiffness of the moment compliance 3/4-ring connecting the cantilever tip to the rigid vertical bars.

Fig. 4 shows the nondimensionalized load cell stiffness versus force on both a linear and log scale. The plots include sample lines for chosen $\frac{PD}{\bar{\delta}_{Max}}$ values that indicate the maximum allowable stiffness of a load cell so that a displacement sensor with the ability to resolve $res_{Sensor} = \frac{2\delta_{Max}}{2^{14}}$ can measure the force within 100P%. Using Eqs. (25) and (36), we nondimensionalize the maximum allowable stiffness of a load cell with 100P% force resolution and a single sensor:

$$K_{SingleSensor} \leq \frac{2^{14}(2F)P}{2\delta_{Max}} \longrightarrow \bar{K}_{SingleSensor} \leq \frac{2^{14}(2\bar{F})P}{2\bar{\delta}_{Max}}. \tag{40}$$

Fig. 5 duplicates the theoretical load cell stiffness versus force plot, but now indicates the maximum allowable stiffness for 100P% force resolution if multiple displacement sensors are allowed so that a load cell with any deflection range can be measured with 0.1 μm resolution. Using Eqs. (26) and (36), we nondimensionalize the maximum allowable stiffness of a load cell with 100P% force resolution and sensors with resolutions of 0.1 μm:

$$K_{MultipleSensors} \leq \frac{2FP}{10^{-7}} \longrightarrow \bar{K}_{MultipleSensors} \leq \frac{2\bar{F}PD}{10^{-7}}. \tag{41}$$

The dependence of the maximum allowable nondimensionalized stiffness on D is due to the dimensionalized resolution of the displacement sensor. Fig. 5 shows that for a surface end-gap of $D = 5$ mm, the load cell satisfies the stiffness requirement for 1% force measurement resolution over a nondimensionalized force range from about $10^{-2} \leq 2\bar{F} \leq 10^4$ (six orders of magnitude).

The load cell stiffness shown in Figs. 4 and 5 is closely related to the contact point values shown in Fig. 3(c). We observe that the load cell with the $n = 2$ surface deflects linearly until the critical force that causes the cantilever to begin contacting the surface. Increasing the value of surface nonlinearity n increases the load cell stiffness for small forces and decreases the stiffness at large forces. This is because a surface with a larger n value more severely interferes with the cantilever's initial deflection (because a surface with a larger n is flatter near the root and rounder near the tip). The resulting larger rate of cantilever-surface contact with increased small forces is shown in Fig. 3(c). For large forces and large contact points, the larger n surface is rounder, and therefore larger increments of force are required to increase the contact point (i.e. make the load cell stiffer).

For the surfaces with $R/L > 0$, once the full cantilever length contacts the surface ($\bar{x}_c = 1$), the load cell stiffness is constant. This is because once the full cantilever is in contact with the rigid surface, further load cell deflection is due to the 3/4-ring deflecting linearly. Increasing R/L decreases the load cell stiffness for all force values because it decreases the stiffness of the moment complaint 3/4-ring at the cantilever's tip. When $R/L = 0$, the full cantilever length does not contact the surface for a finite force. This is because cantilever contact with the surface at $\bar{x} = 1$ would require the cantilever tip to be both tangent to the surface (a nonzero slope) and satisfy the 0-slope requirement of the rigid vertical bar to which it is attached. Since the cantilever of a $R/L = 0$ load cell does not fully contact the surface for a finite force, the stiffness continues to increase for all force values.

Fig. 6 illustrates the stress along the cantilever when the nondimensionalized applied force is $2\bar{F} = 30$. As described by Eq. (19), to the left of the contact point, the stress is proportional to the surface curvature. If the surface nonlinearity power, n equals 2, then the surface curvature is constant, and therefore stress along the beam segment in contact with the surface is also constant. If $n > 2$, then the surface curvature equals 0 at the root and increases along the surface length, so the stress in the cantilever is 0 at the root and increases along the cantilever length. Therefore, the maximum stress occurs at the contact point. Here, we use the sign convention for the top of the cantilever in the South-East 1/4 load cell indicated in Fig. 1 when the load cell is in compression.

The minimum stress in the cantilever (for the plotted $2\bar{F}$ and R/L values) occurs at $\bar{x} = 1$. This is because for the chosen parameter sets, M_{Tip} is positive. Accordingly, Eq. (20) shows that the minimum value of stress in the cantilever will be at $\bar{x} = 1$. Similarly, for these sets of parameters, the minimum value of stress in the entire load cell is at $\phi = \pi/2$ in the 3/4-ring. As described in Section 2.4, changing the ratio of R/L and the force value changes the location of the maximum and minimum stress values in the load cell.

Increasing the surface nonlinearity, n, decreases the stress in the cantilever at small contact point values and increases the stress at larger contact points. This is because the cantilever stress is proportional to the surface curvature at the contact point. As can be seen by differentiating Eq. (1), increasing n decreases the surface curvature at small x values and increases the surface curvature at larger x values. Increasing n also decreases stress in the free cantilever for small contact point values and increases stress in the free cantilever for large contact point values. This is because larger n values make the surface slope smaller at small x values and steeper at larger x values compared to a surface with a smaller n. A cantilever with a larger positive slope at the contact point must have a larger curvature to the right of the contact point so that the slope can equal 0 (or another required smaller slope if $R \neq 0$) at the cantilever tip, as required by the rigid vertical bar (or moment compliance ring).

Increasing R/L decreases the magnitude of the minimum stress in the cantilever at $\bar{x} = 1$. This is because a 3/4-ring with a larger R/L ratio is a weaker rotational spring, and the required change in slope between the contact point and cantilever tip is smaller. Increasing R/L increases the stress at the contact point. This is because the value of the contact point $\bar{x}$ is larger for a given force when R/L is larger because the load cell is weaker. As described in the previous paragraph, the stress at the contact point is always proportional to the surface curvature, which increases with the contact point.

Fig. 7 shows the maximum nondimensionalized stress in the load cell versus force. Fig. 7 accounts for the stress along both the cantilever and 3/4-ring. Increasing n increases the stress for small forces but decreases the stress at large forces (this is caused by the affected rate of contact described above). Fig. 7 shows that the load cell with $R/L = 0.02$ has a change in slope at about $2\bar{F} = 5000$. At this force, the location of the maximum magnitude in the load cell shifts from $\phi = \pi/2$ to $\phi = 3\pi/2$. Further calculations in the location of the maximum stress are described in Section 2.4.

Fig. 8 plots the normalized strain versus force at the cantilever tip, a possible location for a strain gauge. Fig. 8 also plots the strain gradient with respect to the force, which illustrates the force resolution that can be achieved by a strain gauge located at the cantilever tip. Using Eqs. (27) and (39), the the maximum allowable strain gradient of a load cell with 100P% force resolution and a strain measurement resolution of 14-bits nondimensionalizes to:

$$\frac{\mathrm{d}\varepsilon}{\mathrm{d}(2F)} \geq \frac{\varepsilon_{\text{Max}}}{P \times 2^{14}(2F)} \longrightarrow \frac{\mathrm{d}\bar{\varepsilon}}{\mathrm{d}(2\bar{F})} \geq \frac{\bar{\varepsilon}_{\text{Max}}}{P \times 2^{14}(2\bar{F})} \longrightarrow \frac{\mathrm{d}\bar{\varepsilon}}{\mathrm{d}(2\bar{F})} \geq \frac{1}{P \times 2^{14}(2\bar{F})}, \tag{42}$$

where we set $\bar{\varepsilon}_{\text{Max}} = \frac{\varepsilon_{\text{Max}}}{\varepsilon_{\bar{x}_c=0.9}} = 1$ to represent designing the load cell so that the cantilever does not contact the surface beyond $\bar{x}_c = 0.9$, where the strain gauge is located. Fig. 8(a) shows that as n increases, the strain at the cantilever tip for a given force decreases. This is expected because larger n load cells are initially stiffer than smaller n load cells, so a given force causes less deformation. Fig. 8(a) also shows that as R/L increases, the strain at the cantilever tip increases for a given force. This is because larger R/L makes the load cell weaker for small forces and therefore allow more deformation.

Figs. 3–8 can be used to select load cell geometric and material parameters to meet certain performance criteria. Here, we present a case-study of the procedure for designing a load cell that uses one optical sensor, and has a 1% force resolution over applied forces $0.01\text{N} \leq 2F \leq 1000\text{N}$. Fig. 4 indicates that the load cell with $n = 2$, $R/L = 0.01$ satisfies 1% force resolution over the nondimensionalized 5-order-of-magnitude range of $2.2 \times 10^{-2} \leq 2\bar{F} \leq 2.2 \times 10^{3}$, when we set $\frac{D}{\delta_{\text{Max}}} = 1$ (i.e. size the optical sensor for a range of $2\delta_{\text{Max}}$). We choose $n = 2$ because it minimizes the load cell stiffness at small forces compared to larger n surfaces. We choose $R/L = 0.01$ as a trade off between reduced stiffness at low forces (caused by larger R/L) and reduced stress at high forces (caused by smaller R/L). Now, we require that the minimum force dimensionalizes to 0.01 N:

$$2F_{\text{Min}} = \frac{3EID(2\bar{F}_{\text{min}})}{L^3} \longrightarrow 0.01 = \frac{Ebt^3D(2.2 \times 10^{-2})}{4L^3}. \tag{43}$$

We also require that the load cell satisfies the maximum allowable stress at the maximum force. Fig. 7 shows that the $n = 2$, $R/L = 0.01$ load cell has a nondimensionalized stress value of $\bar{\sigma} = 34.5$ when $2\bar{F} = 2.2e3$, which dimensionalizes to

$$\sigma_{\text{Max}} \leq \frac{\bar{\sigma}DtE}{L^2} = \frac{34.5DtE}{L^2}. \tag{44}$$

We use Eqs. (43) and (44) to choose values for the load cell's geometric and material parameters: elastic modulus E, cantilever width b, thickness t, length L, and surface end-gap D. We choose to make the load cell out of aluminum, with an elastic modulus of $E = 70$ GPa and maximum allowable stress of $\sigma_{\text{Max}} = 200$ MPa for a near-infinite fatigue life. We also set $L = 15$ cm, $b = 5$ mm, and $D = 2$ mm as reasonable limits to the load cell size and machining accuracy constraints. Then, Eqs. (43) and (44) are satisfied when $t = 0.4$ mm.

3. Fabrication

We fabricated the mechanical components of the load cell from one monolithic piece. The advantages of a monolithic load cell compared to a load cell assembled from several parts are reduced assembly cost and elimination of the hysteresis often caused by bolts. One can fabricate a monolithic load cell by 3D printing, milling, or waterjetting. We chose waterjetting because of its high precision and ability to make small-diameter cuts.

A limitation when using the waterjet (or mill) is that the machine cannot cut to an exact point where the cantilever and surface roots meet, as shown in Fig. 1, because the water jet (or end mill) has a minimum hole diameter that it can cut.

Here, we describe two solutions to overcome this limitation. First, we design gaps in the surfaces near their roots to satisfy the minimum cut that the machine can make in between the surface and cantilever, as shown in Fig. 9. We design the gaps to extend to the minimum required distance along the surface axes to minimize their effect on the theoretical load cell performance. Before contacting the surface, the load cell deflects linearly. This means that for small forces, the load cell remains at its initial stiffness instead of stiffening, which is actually beneficial for measuring small loads because larger deflections are measured more accurately by the sensor. Developing the analytic theory for how the load cell behaves with the root gaps rather than surfaces extending to the cantilever roots results in long, complicated expressions. If properly designed, the effects of these gaps should be minimal on the theory, as seen in the experimental results described in Section 4.

A second fabrication option is to machine inserts (with a 0.25 mm clearance) that can be adhered into the root gaps, as shown in Fig. 9. This allows the surface to effectively meet the cantilever root at a point, which is required for nonlinear load cell behavior at small forces.

We fabricated two prototype load cells. The first load cell has cantilever tips that directly connect to the rigid vertical bars ("rigid connections"). Load cell geometry prevents deflection exceeding

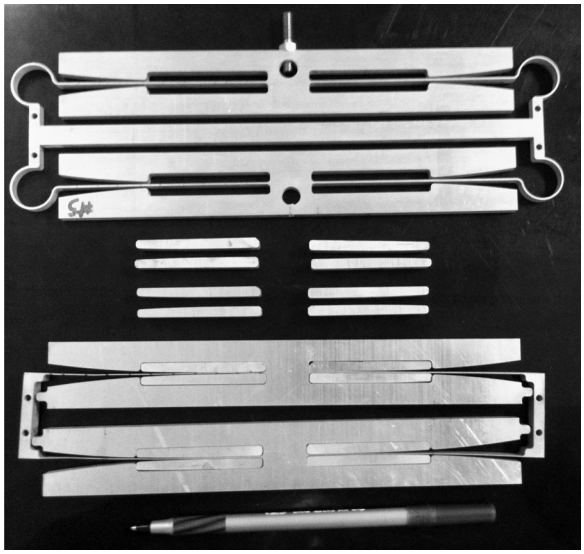

Fig. 9. Fabricated aluminum load cells. Top: Load cell with moment compliant 3/4-rings and a horizontal crossbar without inserts. Middle: Inserts. Bottom: Load cell with rigid connections and root inserts in the root gaps.

8 mm in both tension and compression in order to keep the stress in the flexures below 200 MPa: in compression, the top and bottom rigid blocks contact each other at 8 mm deflection. In tension, the overstops, labeled in Fig. 1, prevent over-deflection. This load cell was cut from a 9.52-mm thick sheet of 6061 aluminum using an Omax 2626 abrasive waterjet machine with a tilt-a-jet head for achieving near-zero taper. This waterjet can cut to an accuracy of 0.076 mm and make cuts as thin as 1 mm thick.

The second load cell has moment compliance flexures connecting the cantilever tips to vertical rigid bars. These flexures are physically realized by 270° arcs ("3/4-rings") with radii of $R = 1$ cm. The rigid blocks prevent the load cell from deflecting beyond 10 mm in compression. Although we did not include tension overstops in this prototype, they may be added to the rigid blocks as shown in Fig. 1.

This second load cell prototype also has a rigid horizontal crossbar connecting the left and right rigid vertical bars to reduce parasitic rotations and horizontal deflections. The horizontal bar stiffens the load cell against parasitic moments and horizontal deflections because some of these parasitic motions require the vertical rigid bars to rotate with respect to each other. We note that a challenge in implementing this stiffener is that the load cell should have minimized weight in order to measure small forces in a vertical configuration. To address this issue, we propose cutting holes in the crossbar and in the middle of the surfaces in order to minimize their masses while maintaining their effective infinite stiffness.

This second load cell was cut from a 6.35-mm thick sheet of 6061 aluminum using an Omax MicroMAX waterjet machine, which has a position accuracy of 15 μm and cut the sheet with a taper less than 0.057°.

The load cell with rigid connections has a cantilever thickness $t = 0.5$ mm and a cantilever width $b = 9.52$ mm. The load cell with moment complaint rings has a cantilever thickness $t = 1$ mm and a cantilever width of $b = 6.35$ mm. Both load cells have the following parameters: cantilever and surface lengths, $L = 10$ cm, surface nonlinearity $n = 3$, maximum surface gap $D = 5$ mm, elastic modulus $E = 65e9$ Pa, and maximum allowable stress $\sigma_{Max} = 200$ MPa.

As per the first solution for fabricating the load cell out of one monolithic part, we designed gaps in the surfaces that extend from the cantilever root to the axial coordinate, x_{Gap}, where the distance between the surface and undeflected cantilever is $S_{Gap} = 1$ mm. For surfaces that follow the curve $S = D(x/L)^n$, the axial coordinate corresponding to a chosen distance between the undeflected cantilever and surface is $x_{Gap}/L = (S_{Gap}/D)^{1/n}$. For the chosen prototype parameters, each gap extends from the cantilever root to $x_{Gap} = 58$ mm $x_{Gap}/L = 0.58$.

Based on the theory in Section 2, when the load cell has rigid connections and the surfaces extend the full cantilever length, the force (deflection) for which the $x_c = 0.58$ mm is 1.0 N (5.5 mm), which is 1.1% the force (60% the deflection) required for 95% of the cantilever length to be in contact with the surface. With the root gaps, the first contact between the cantilever and surface at $x = 58$ mm is 0.12 N. For the load cell with 3/4-ring connections and surfaces that extend the full cantilever length, $x_c = 58$ mm when the force (deflection) is 3.8 N (9.7 mm), which is 17% the force (65% the deflection) required for 95% of the cantilever length to be in contact with the surface. With the root gaps, the first contact between the cantilever and surface is at 0.40 N. After contact occurs at $x/L = 0.58$ when the root gaps are present, we expect the cantilever to pivot at the contact point as additional force is applied until the cantilever is tangent to the surface at that point.

We experimentally verify the effectiveness of these two fabrication methods in Section 4.

4. Experimental verification

We performed quasi-static force versus displacement tests to verify the theory described in Section 2 and show the effectiveness of the fabrication methods described in Section 3. We performed these tests on two fabricated load cells: one with rigid vertical bar connections and one with moment compliant 3/4-ring connections, using and not using inserts in the root gaps, in both tension and compression modes, as shown in Fig. 9. For the load cell with 3/4-ring connections, we performed cyclic loading to measure the load cell's hysteresis.

The load cells were made out of 6061 aluminum with the dimensions listed in the captions of Figs. 11 and 12.

The tests used an Interface SMT1 load cell with a 2.2 lbf capacity on an ADMET eXpert 5000 force tester machine with the single-column vertical set-up shown in Fig. 10. The load cell recorded force with a resolution of 1×10^{-4} N and the ADMET recorded displacements with a resolution of 1×10^{-4} mm. The nonlinear load cell top was bolted to the Interface load cell, and the nonlinear load cell bottom was bolted to the tabletop.

For the nonlinear load cells and force tester machine that were readily available, bolting both the top and bottom of the nonlinear load cell made the experimental set-up slightly overconstrained. The bottom fixture did not perfectly align with the top fixture. Gripping both ends of the load cell was required for the tension test. As described below, this overconstraint affected the experimental results of the load cell with rigid connections. It played less of a role for the load cell with the 3/4-ring connections because the horizontal crossbar made it more robust to parasitic moments and horizontal forces. A future solution for this experimental set-up is to fabricate the load cells with holes through which close-fitting pins can transmit the applied forces.

For the given experimental set-up, we determined the zero-deflection point of the load cell by symmetry in the force versus deflection curve. The zero-deflection point of the load cells was not obvious because gravity compressed the unloaded load cells. Further, any slight misalignment between the top and bottom fixtures made using the maximum compression point of the load cell an unreliable deflection reference point.

We performed five trials for each load cell configuration and determined the mean experimental force at each displacement.

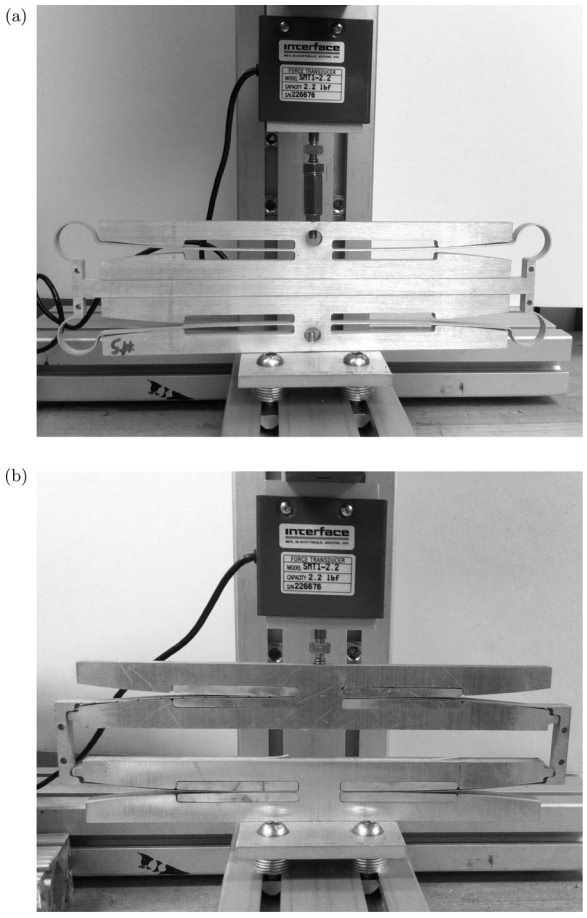

Fig. 10. (a) Force versus displacement experimental set-up of load cell with moment compliance 3/4-ring connections without inserts, in maximum compression. (b) Load cell with rigid connections in maximum tension with inserts.

Fig. 11 compares the mean experimental force versus displacement to the theory for the load cell with rigid connections. As shown in Fig. 11, we designed the load cell to have a maximum allowable deflection of 8 mm in both tension and compression in order to keep the maximum stress in the load cell below 200 MPa. Fig. 12 compares the mean experimental force versus displacement to the theory for the load cell with moment complaint 3/4-ring connections. As shown in Fig. 12, we designed this load cell to have a maximum allowable deflection of 10 mm so that the maximum stress in the load cell remained below 200 MPa. Among all of the experiment variations (load cell with rigid or 3/4-ring connections, with or without root inserts, in tension or compression), the standard deviation in the measured force for a given measured deflection was less than 0.05% and occurred at small deflection values (near 2 mm) in compression for the load cell with 3/4-ring connections. For all other measurements, the standard deviation was less than 0.005%.

We observed very good agreement between the experiments and theory for the load cell with rigid connections in compression both with and without inserts up to 6 mm deflection (after which, slight set-up misalignment caused overstop behavior earlier than theoretically expected, as discussed below). Tests for the load cell with rigid connections in tension both with and without inserts followed a close trend with the theory as well except for being slightly stiffer than theoretically expected at midrange displacements. We observed very good agreement between the experiments and theory for the load cell with 3/4-ring connections with inserts in compression mode. The load cell with 3/4-ring

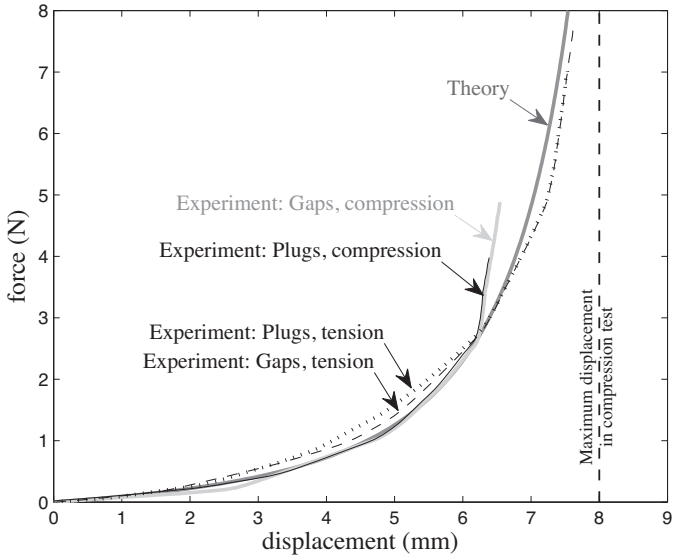

Fig. 11. Force versus displacement test results for the aluminum load cell with rigid connections. The load cell parameters were: cantilever and surface lengths, $L = 10$ cm; cantilever thickness, $t = 0.5$ mm; cantilever width, $b = 9.5$ mm; surface curve power $n = 3$; maximum surface gap, $D = 5$ mm; elastic modulus, $E = 65$ GPa; maximum allowable stress, $\sigma_{all} = 200$ MPa.

connections with inserts in tension mode also generally followed the theory except for a midrange-deflection error that showed a slightly higher force than expected and linear behavior. Tests for the load cell with 3/4-ring connections with the root gaps in both compression and tension modes showed larger initial linear regimes than expected.

As described in Section 3, when the surfaces have root gaps, we theoretically expect the load cell with rigid connections to deflect linearly with a stiffness of 97.8 N/m until 0.12 N has been applied. As illustrated in Fig. 11, the experimental results showed that the load cell deflected with an initial stiffness of 78.2 N/m until 0.19 N was

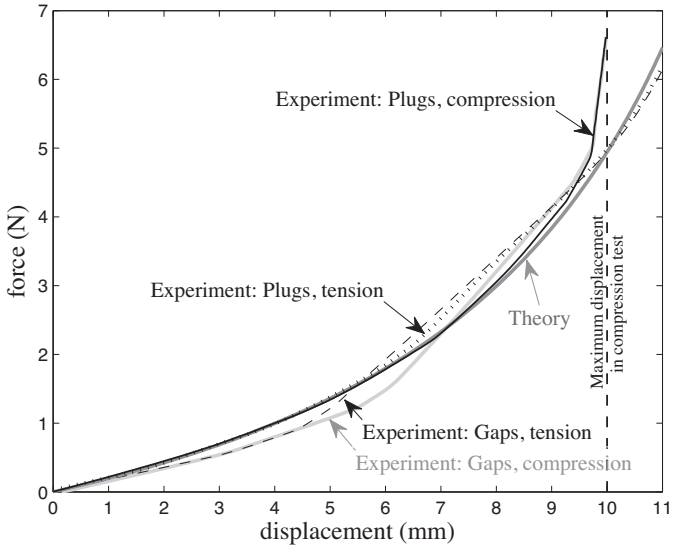

Fig. 12. Force versus displacement test results for the aluminum load cell with moment compliant "3/4-ring" connections. The load cell parameters were: cantilever and surface lengths, $L = 10$ cm; cantilever thickness, $t = 1$ mm; cantilever width, $b = 6.3$ mm; surface curve power $n = 3$; maximum surface gap, $D = 5$ mm, rotational spring radius, $R = 1$ cm; elastic modulus, $E = 65$ GPa; maximum allowable stress, $\sigma_{all} = 200$ MPa.

applied in tension mode and with a stiffness of 98.3 N/m in compression mode until 0.20 N was applied. We theoretically expect the load cell with 3/4-ring connections to deflect linearly with a stiffness of 166.7 N/m until 0.40 N is applied. As illustrated in Fig. 12, the experimental results showed that the load cell deflected with an initial stiffness of 165.2 N/m in tension mode until 1.2 N was applied and with a stiffness of 188.3 N/m in compression mode until 0.96 N was applied. These differences were most likely due to slight misalignment in the experimental set-up as described below.

We observed three main errors between the experiment and theory:

1. The load cell with rigid connections in tension was initially stiffer than what is predicted by the theory. The load cell with root gaps in tension mode had a maximum error from the theory of 0.32 N (29%) at a deflection of 4.8 mm.
2. The load cell with rigid connections in compression had a sudden change in stiffness at a deflection of 6 mm, due to the top and bottom rigid surfaces touching each other and overstopping the load cell 2 mm earlier than expected.
3. The load cell with 3/4-ring connections and root gaps deflected linearly in both tension and compression modes even after contacting the beginning of the surface ($x_c = 0.58$ mm) rather than behaving nonlinearly.

We provide several explanations for these and the other smaller discrepancies between the theory and experiment.

Error 1, the discrepancy between the theoretical and experimental stiffnesses for the load cell with rigid connections in tension in Fig. 11, may have been due to two key issues.

First, the slightly overconstrained experimental set-up induced parasitic moments and horizontal forces on the load cells. Misalignment caused the four load cell quadrants to deflect asymmetrically, while the theory assumes that the load cell deflects symmetrically. Asymmetry caused each of the cantilevers to have different contact points and therefore different effective stiffnesses at a given force. We observed that adding a horizontal crossbar, as was done for the load cell with 3/4-ring connections, made the load cell more robust to parasitic loadings.

Second, the Omax 2626 did not cut the cantilevers of the load cell with rigid connections to a constant thickness along their lengths as specified by the SolidWorks CAD. This error may have been caused by not correctly compensating for the kerf width in between the cantilever and surface or vibrations during cutting. We used calipers to make 10 evenly-spaced measurements along the cantilever length on both the front and back of each load cell. Here, "front" refers to the side of the aluminum sheet that was face-up while being waterjetted. We found that the front of the load cell, which had a nominal cantilever thickness of 0.5 mm, had a mean thickness of 0.49 mm and standard deviation of 0.05 mm. We found that the back of the cantilever had a larger mean thickness of 0.55 mm and standard deviation of 0.03 mm. The different mean thicknesses of the front and back of the load cell indicated a tapered cut by the waterjet machine, despite using the tilt-a-jet head. The surfaces to which the cantilevers become tangent had a similar taper which may have reduced any torsional effects in the cantilever due to its mean taper. The thickness values fluctuated randomly along the cantilever length except for a bump on the back of the cantilever at $x = 58$ mm, where the root gap ended and the distance between the surface and cantilever was at its minimum value of 1 mm. At $x = 58$ mm, the cantilever's back thickness had its largest value of 0.64 mm, and then the thickness decreased back to its mean value 10 mm further along the cantilever. All four cantilevers of the load cell showed this bump in thickness at $x = 58$ mm.

The bump in cantilever thickness at $x = 58$ mm affected the rate of increase in the cantilever-surface contact point for increased forces. As described in the Section 2, the increasing stiffness of the load cell is highly dependent on the rate of increase of the contact point (i.e. increasing the contact point shortens the free cantilever segment and increases the load cell stiffness). Developing the theory of how the contact point relates to the applied force for a cantilever with non-monotonically varied thickness is beyond the scope of this paper. However, we expect a bump to cause the load cell contact point to initially increase by a larger amount than predicted for a smooth cantilever because the bump contacts the surface before a smooth cantilever would contact the surface. This causes the load cell stiffness to increase more for a given force increase than if it had a smooth cantilever. After the apex of the bump has contacted the surface, we expect the contact point to increase at a slower rate than predicted for a smooth cantilever because the bump creates a separation between the rest of the surface and free cantilever. This, in turn, causes the load cell stiffness to increase at a slower rate as more force is applied compared to a smooth cantilever.

The load cell with moment compliant 3/4-ring connections, which had a nominal cantilever thickness of 1 mm and was cut on the Omax MicroMax had much more consistent cantilever thicknesses, with a mean value of 1.03 mm on the front, 1.04 mm on the back, and standard deviation of 0.03 mm among all of the measurements.

Slight experimental set-up misalignment contributed to the second error between the experiment and theory, for which the experimental force suddenly increased to values significantly larger than expected for the load cell with rigid connections in compression. This sudden increase in force was caused by the top and bottom rigid blocks of the load cell contacting each other. In the experiment, a slight angle in the top rigid block caused the left side of the rigid blocks to contact each other before the right side. Theoretically, when the rigid blocks have 100 mm lengths on either side of the fixture, the top rigid block left edge may first contact the bottom block left edge at 6 mm deflection instead of 8 mm deflection if the relative angle between them is as small as 1.14°. The theoretical load cell model assumes simultaneous contact of the entire planes of the rigid blocks.

Error 3 between the experiment and theory, for which the load cell with 3/4-ring connections with root gaps deflected with two linear regions instead of showing nonlinear behavior, can be seen in Fig. 12. This error was caused by the cantilever pivoting about the contact point at the start of the surface ($x_c = 0.58$ mm) rather than increasing the contact point as the force was increased. The theory for how the load cell deflects when its contact point pivots around the start of the surface with root gaps at $x_c = 58$ mm is beyond the scope of this paper. However, the experimentally observed constant slope of 889 N/m for compression mode and 799 N/m for tension mode were within 18% of the load cell stiffness of 973 N/m that is predicted by the theory when the surface does not have the root gaps and the contact point is $x_c = 0.58$ mm. When the contact point is $x_c = 0.58$ mm and the load cell has root gaps, then we expect its stiffness to be less because the cantilever pivots at the contact point.

Finally, we note that averaging among the four load cell quadrant stiffnesses may have reduce manufacturing and asymmetry errors. For example, in a vertical set-up, when the load cell had a horizontal crossbar that weighed 0.37 N, all four cantilevers sagged downward. This, in turn, caused the contact point of the upper cantilevers to be slightly less than that of the lower cantilevers when the load cell was in compression mode. When the load cell was in tension mode, the contact point of the upper cantilevers was slightly larger than that of the lower cantilevers. In these situations, while the effective stiffness of two quadrants was higher than theoretically expected, the effective stiffness of the other two quadrants was lower than expected, and the overall result

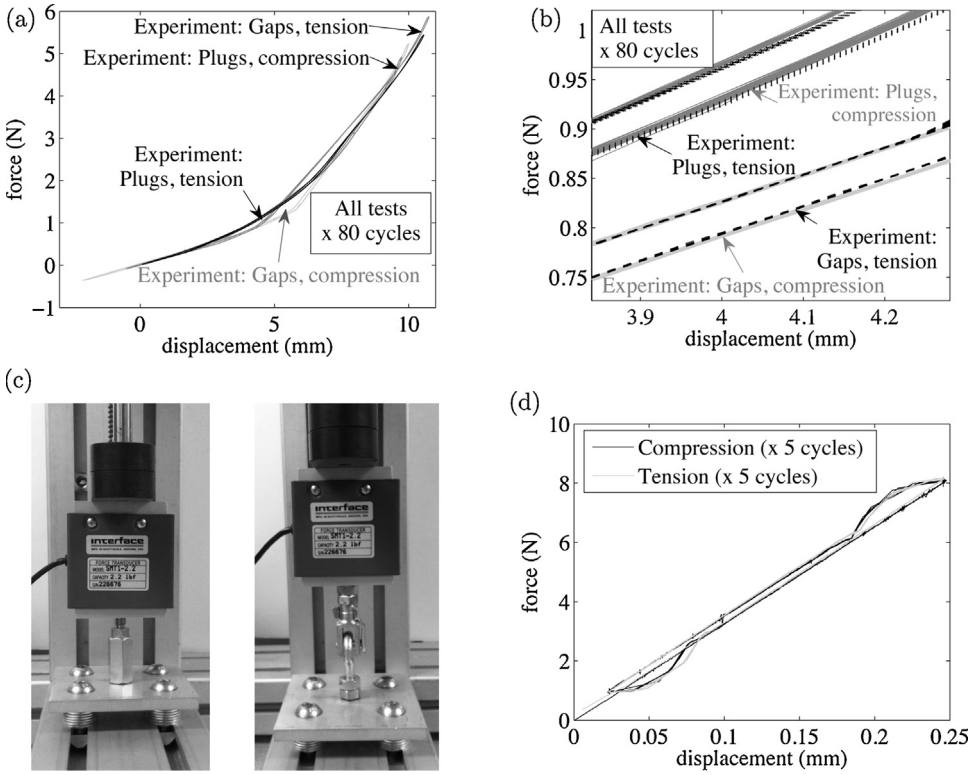

Fig. 13. Hysteresis tests. (a) Experimental results for load cycling for the load cell with moment compliant "3/4-ring" connections. (b) Closer look at experiment results of (a). (c) Experimental set-up for measuring hysteresis in the experimental set-up. Left, compression set-up. Right, tension set-up. (d) Measured hysteresis in the ADMET force tester experimental set-up.

was only a moderate effect on the stiffness of the load cell as a whole.

4.1. Hysteresis in the load cells

For the load cell with 3/4-ring connections, we performed cyclic loading from near-minimum to near-maximum load to measure the hysteresis in the load cell. The cycles were repeated 80 times for each load cell configuration (compression or tension mode, with or without inserts). The results are shown in Fig. 13. Overall, the results suggest that the load cells have little hysteresis.

First, we determined any hysteresis in the experimental set-up that was not caused by the nonlinear load cell. For this simple test, we used the set-up shown in Fig. 13c. Neglecting the extra large regions of displacement hysteresis at the cycle extremities, we measured that the ADMET machine itself showed an average difference of 0.0071 mm between the increasing and decreasing deflection magnitudes. We suspect that the hysteresis was due to the backlash of bolts or gears. In the paragraph below describing hysteresis in the nonlinear load cell, we subtract the 0.0071 mm from the deflection differences.

Among all of the cyclic data sets, the maximum difference between the increasing and decreasing deflection magnitudes at a given force was 0.1750 mm and occurred for the load cell in tension mode without inserts at a nominal force of 0.57 N (nominal deflection of 2.956 mm, increasing magnitude). The load cell in tension with inserts showed a maximum deflection difference of 0.0850 mm at 2.2 N. The load cell in compression without inserts showed a maximum deflection difference of 0.1409 mm at 1.34 N. The load cell in compression with inserts showed a maximum deflection difference of 0.0955 mm at 2.19 N.

To work as an actual product, it is important to account for these deflection differences due to hysteresis. As an example of the issues that arise due to the combined hysteresis and nonlinearity, we consider the measurement errors that arise if the load cell prototype with 3/4-ring connections has a hysteretic deflection jump of 0.11 mm. When the force is increasing, the load cell deflects 1.50 mm when 0.30 N is applied. When the force is decreasing and 0.30 N is applied, the load cell deflects 1.61 mm due to hysteresis. If the sensor is calibrated solely for increasing force magnitudes, then it will correlate the 1.61 mm deflection to 0.333 N, which is a force overprediction of 11%. At a larger force, when 4.45 N is applied and the force is increasing, the load cell deflects 9.60 mm. When the force is decreasing and 4.45 N is applied, the load cell deflects 9.71 mm due to hysteresis. If the sensor is calibrated solely for increasing force magnitudes, then it will correlate the 9.71 mm deflection to 4.635 N, which is a force overprediction of 3.7%.

It may be possible to design the load cell so that measurement errors due to hysteresis remain below a certain force percentage. Also, we suggest that the software used to correlate a deflection sensor reading to a force account for whether the measured force is along an increasing or decreasing force trajectory.

5. Conclusions and future work

A load cell with increasing stiffness has a larger force measurement resolution and force range than a traditional linear load cell. We physically implemented a stiffening load cell by designing cantilevers to increasingly contact rigid surfaces (and therefore have effectively shorter lengths) as additional force is applied. We reduced stress in the load cell by combining cantilevers with moment compliant 3/4-rings that act like rotational springs. Rigid surfaces and overstops prevented the load cell from breaking for forces beyond the load cell's force range. A horizontal crossbar reduced the load cell's susceptibility to parasitic moments and horizontal forces.

We investigated parameters that allow the nonlinear load cell to measure forces with resolutions of 1% of the applied force over a 5-orders-of-magnitude force range. High resolution was achieved by designing the nonlinear load cell's stiffness to remain below values that allow a sensor to detect the deflection change corresponding to a 100P% change in the force, where P is the chosen sensor resolution.

Additionally, we described a method of fabricating the load cell out of one monolithic part, which reduces assembly costs and the hysteresis caused by bolts. While machines such as the waterjet and mill cannot cut the theoretical point-junction of the beam and surface, machining gaps in the surface near the cantilever root and separate inserts can effectively create the point-junctions.

We experimentally verified the nonlinear load cell theory and showed the effectiveness of the fabrication method for two different sets of load cell parameters. The experimental force-deflection curves when inserts fill the root gaps effectively matched the force-deflection curve when the inserts were not used. Manufacturing the load cell with gaps that do not need to be filled by inserts further reduces the load cell manufacturing cost. We observed high sensitivity of the load cell nonlinearity to the accuracy of the cantilever and surface cuts.

Future work on this project will include experimentally verifying the theory with a load cell designed to function over several orders of force magnitude. Additionally, we will investigate optimizing the load cell when the cantilever and 3/4-ring parameters are allowed to vary along their lengths, x and ϕ, respectively. We will also work on investigating a nonlinear load cell that implements the flexure-contact surface stiffening effect in a more volume efficient way. Also, we will characterize the dynamic behavior of the nonlinear load cell, which is important for applications such as load platforms.

Finally, we note that a future important step is determining how to best attach a sensor to the nonlinear load cell and calibrate it for measuring unknown forces. We suggest that a favored calibration method should be to use an instron machine such as the ADMET force tester with multiple high-accuracy linear load cells that span the entire range of the nonlinear load cell. Several thousand (force, deflection) data points could be used to correlate a load cell deflection to a force. If the load cell shows different force-deflection curves in tension mode than in compression mode, then these modes may be calibrated separately. This future calibration work will also include ensuring that the zero-deflection reference point is easily determined, which is highly important for a nonlinear load cell. We will investigate determining the zero-deflection point by using root gaps, which cause an abrupt change in load cell stiffness at a specific deflection, or simply using deflection sensors with minimal drift.

Acknowledgements

We are grateful to Wesley Cox for his assistance in the experiments. We also gratefully acknowledge the Naval Engineering Education Center for support under Grant No. 3002883706, the National Science Foundation for support of JMK through the Graduate Research Fellowship Program under Grant No. 1122374, and the MIT Energy Initiative through the project 'Efficient nonlinear energy harvesting from broad-band vibrational sources by mimicking turbulent energy transfer mechanisms'. Patents have been filed based on the research results presented in this manuscript.

References

[1] Sanders J, MIller R, Berglund D, Zachariah S. A modular six-directional force sensor for prosthetic assessment: a technical note. J Rehabil Res Dev 1997;34(2):195–202.
[2] Mokhbery J. Advances in load cell technology for medical applications. Medical Device and Diagnostic Industry newsletter; 2014 [accessed online September].
[3] Change Y-S, Lin T-C. An optimal g-shaped load cell for two-range loading. Eng Agric Environ Food 2013;6(4):172–6.
[4] Mantriota G, Messina A. Theoretical and experimental study of the performance of flat suction cups in the presence of tangential loads. Mech Mach Theory 2011;46(5):607–17.
[5] Cordero A, Carbone G, Ceccarelli M, Echavarri J, Munoz J. Experimental tests in human robot collision evaluation and characterization of a new safety index for robot operation. Mech Mach Theory 2014;80:184–99.
[6] Smith J. Electronic scale basics. Key Markets Publishing; 1991.
[7] Limited OE. An introduction to load cells, history, theory & operating principles; 2014 http://www.omega.co.uk/prodinfo/load-cells.html
[8] Acuity. Principles of measurement used by laser sensors; 2014 http://www.acuitylaser.com/support/measurement-principles
[9] Lion. Understanding sensor resolution specifications and effects on performance; 2014 http://www.lionprecision.com/tech-library/technotes/article-0010-sensor-resolution.html
[10] Microtrack 3. Tech. rep. MTI Instruments; 2014.
[11] Storace A., Sette P. Leaf spring weighing scale, U.S. patent US4037675.
[12] Suzuki S., Nishiyama Y., Kitagawa T. Multi-range load cell weighing scale, U.S. patent US4711314.
[13] McFarland D, Bergman L, Vakakis A. Experimental study of non-linear energy pumping occurring at a single fast frequency. Int J Non-Linear Mech 2005;40:891–9.
[14] Hajati A, Bathurst S, Lee H, Kim S. Design and fabrication of a nonlinear resonator for ultra wide-bandwidth energy harvesting applications. In: Proceedings of the IEEE International Conference on Micro Electro Mechanical Systems (MEMs). 2011. p. 1301–4.
[15] Mann B, Sims N. Energy harvesting from the nonlinear oscillations of magnetic levitation. J Sound Vib 2009;319:515–30.
[16] Kantor Y, Afanas'eva L. Nonlinear flexure of a circular plate of variable thickness. Prikl Mekhanika 1968;4(7):71–4.
[17] Timoshenko S. Strength of materials. Van Nostrand; 1955.
[18] Kluger J, Sapsis T, Slocum A. Enhanced energy harvesting from walking vibrations by means of nonlinear cantilever beams. J Sound Vib 2015;341:174–94.
[19] Kluger J. Nonlinear beam based vibration energy harvesters and load cells. Massachusetts Institute of Technology; 2014 [Master's thesis].
[20] Young WC, Budynas RG. Roark's formulas for stress and strain. McGraw-Hill; 2002.